COPYRIGHT NOTICE

Federation UNIVERSITY • AUSTRALIA

FedUni ResearchOnline
https://researchonline.federation.edu.au

This is the submitted version of the following article:

Song, C., Ooi, E. T., & Natarajan, S. (2018) A review of the scaled boundary finite element method for two-dimensional linear elastic fracture mechanics. *Engineering Fracture Mechanics*, *187*, 45-73.

Which has been published in final form at:
https://doi.org/10.1016/j.engfracmech.2017.10.016

Copyright © 2016 Elsevier Ltd.

A review of the scaled boundary finite element method for two-dimensional linear elastic fracture mechanics

Chongmin Song[a,*], Ean Tat Ooi[b], Sundararajan Natarajan[c]

[a]*School of Civil Environmental Engineering, University of New South Wales, Sydney NSW 2052, Australia*
[b]*Federation University, Australia*
[c]*Integrated Modelling and Simulation Lab, Department of Mechanical Engineering, Indian Institute of Technology-Madras, Chennai, India.*

Abstract

The development and the application of the scaled boundary finite element method for fracture analysis is reviewed. In this method, polygonal elements (referred to as subdomains) of arbitrary number of edges are constructed, with the only limitation that the whole boundary is directly visible from the scaling centre. The element solution is semi-analytical. When applied to two-dimensional linear fracture mechanics, any kinds of stress singularities are represented analytically without local refinement, special elements and enrichment functions. The flexibility of polygonal elements in geometric shape leads to simple yet efficient remeshing algorithms to model crack propagation. Coupling procedures with the extended finite element method, meshless method and boundary element method to handle changes in the crack morphology have been established. These developments result in an efficient framework for fracture modelling. Examples of applications are provided to demonstrate their feasibility.

Keywords: crack propagation; interface crack; scaled boundary finite element method; stress intensity factors; T-stress

1. Introduction

Within the framework of linear elasticity, stress singularities exist at crack tips, V-notches, re-entrant corners and free edges formed by dissimilar materials [1, 2, 3, 4]. The best known case of stress singularity is a crack in a homogeneous isotropic body. The asymptotic analytical solution reported in the literature [1, 5] illustrates the proportionality of the stress to $r^{-\frac{1}{2}}$ (square-root singularity), where r is the distance measured from the crack tip. When the crack is on the interface between two dissimilar materials, the stress singularities are of the order $r^{-\frac{1}{2}+i\varepsilon}$ [6, 7, 8], where $i=\sqrt{-1}$ is the imaginary unit and ε is an oscillatory index depending on the ratio of the material properties. Two of the important parameters that describe the state of stress within the framework of two-dimensional linear elastic fracture mechanics are the mode I and mode II stress intensity factors, K_I and K_{II}. In case of interface cracks, the two stress intensity factors are always coupled and often expressed as K_I+iK_{II} [9, 10]. When the two dissimilar materials are isotropic, the singular stress field depends on three parameters: K_I, K_{II} and ε. Furthermore, when the materials are anisotropic [11, 12], two additional parameters are needed to describe the singular stress field. V-notches, free edges,

*Corresponding author. Tel.: +61 2 9385 5021; fax: +61 2 9385 6139.
Email address: c.song@unsw.edu.au

re-entrant corners and other two dimensional problems of stress singularities can be regarded as particular configurations of a multi-material corner. The asymptotic solution of the singular stress field at a multi-material corner is very complex [13, 14], and more than two singular stress modes may exist. Hence, an accurate and efficient modeling of singular stress fields is necessary for the application of linear elastic fracture mechanics to engineering analysis and design.

The finite element method has evolved to be a robust and industry-accepted numerical method for engineering analysis and design. However, the presence of singularities poses challenges. Adding to the complexity of computational fracture modelling is the problem of crack propagation. This is because the finite element method:

- employs polynomial-based interpolation functions that do not resemble the singular stress field.
- requires a conforming mesh topology. As a result, the mesh needs to be updated to account for the changing crack morphology.
- requires additional post-processing techniques to extract the stress intensity factors [2, 15].

The aforementioned difficulties can be circumvented by improving the approximation capability of the finite element method. For example, the singular stress field is modelled by refining the mesh in the vicinity of the cracks or by using special types of elements, such as quarter-point elements [16, 17]. In case of quarter-point elements, the singularity is captured by the virtue of the location of the mid-side node with respect to the crack tip. A conforming mesh is handled using sophisticated remeshing algorithms e.g. [18, 19, 20, 21]. The sophistication involved is related to the requirement of a fine mesh or the use of special elements in the vicinity of the crack tip so that the singular stress field in the locality can be accurately determined. The restriction of the finite element library, which consists of only triangular and quadrilateral elements (in two dimensions), also contributes to the complexity in developing remeshing algorithms. From the perspective of computational effort, the use of remeshing algorithms coupled with the need of a fine mesh in the vicinity of the crack tip is not efficient as they together consume the bulk of the computational time in crack propagation simulations. The fracture parameters are computed by employing special techniques such as path-independent integrals [22, 23], virtual crack closure technique [24], hybrid-element approach [25, 26, 27], Irwin's crack closure integral [28], to name a few. Tracey [29] and Atluri et al. [30] proposed a hybrid formulation that has an inverse square-root singularity near the crack tip. The salient feature of this approach is that it does not require additional post-processing techniques to estimate the stress intensity factors. Although, the above approaches are considered to be major milestones in applying the finite element method to linear elastic fracture mechanics, they still require a conforming mesh (which could be tedious in case of cracks in three dimensions, or when there are multiple cracks even in two dimensions). Moreover, the interaction integrals have to be specifically formulated when applied to different types of materials e.g. functionally graded materials [31, 23].

In a continued effort to alleviate the limitations of the finite element method, several techniques have been proposed, such as the meshfree method [32, 33, 34, 35] and the extended finite element method [36, 37, 38]. The meshfree method, as the name suggests, does not require a pre-defined mesh topology. This makes it attractive to handle crack morphology changes when the crack propagates. This is accomplished by adding a new pair of nodes to represent the

newly formed crack surfaces as the crack propagates. On another related front, the extended finite element method represents the discontinuities, such as cracks or material interfaces, implicitly. This is done by augmenting the conventional finite element approximation basis with *a priori* known functions that can capture the local behaviour. For example, a Heaviside function is used to represent the jump across the crack face and asymptotic functions are incorporated to capture the singular field in the vicinity of the crack tip. The salient feature is that it does not require special elements (e.g., quarter-point elements) or mesh adaptation techniques to represent stress singularities and surface discontinuities. Both the meshfree method and the extended finite element method have a common goal, ie., reducing the meshing burden in computational mechanics. Of particular interest is the extended finite element method, because it is built on the finite element framework and could be combined with any existing finite element codes. The extended finite element method has already been implemented in commercial software such as Abaqus and Ansys. The fracture parameters are computed by either using path-independent integrals or by Irwin's crack closure technique. Xiao and Karihaloo [25, 27, 39] employed a hybrid technique within the framework of the extended finite element method, thus facilitating the computation of stress intensity factors without additional post-processing. The success of the extended finite element method, however, relies on the *a priori* knowledge of the functions that augment the finite element basis, so that the enriched approximation can capture the local behaviour accurately. Many fracture problems have been successfully modelled by both the meshfree method and the extended finite element method [40, 41, 42]. Despite their success in eliminating the need for remeshing, both the extended finite element method and the meshfree method introduce other numerical difficulties in fracture simulations such as the need for special integration techniques in the enriched regions in the extended finite element method; imposition of essential boundary conditions [32, 43] and inaccuracies in defining the crack geometry [33, 34] in the meshfree method. Many techniques have been proposed to address these difficulties such as the use of level sets in conjunction with the meshfree method [44]. Various techniques to resolve the integration of the stiffness matrix of enriched elements in the extended finite element method were discussed in detail by Richardson et al. [45]. The above mentioned techniques can be classified as domain based approach. An alternative to this is the boundary based approach, viz., the boundary element method [46] and the symmetric Galerkin boundary element method [47, 48]. The boundary element method reduces the computational complexity of the problem by reducing the spatial dimensions by one, because only the boundary needs to be discretised. However, it requires the existence of Green's function in order to formulate a solution.

Another major milestone is the introduction of the scaled boundary finite element method [49, 50]. This semi-analytical approach combines the best features of the domain based approaches such as the finite element method and the boundary based approaches such as the boundary element method. It reduces the spatial dimensions of the problem by one as in the boundary element method and like the finite element method, it does not require the knowledge of Green's function. The method relies on the definition of a new coordinate system, referred to as "*the scaled boundary coordinate system*", that decomposes the usual Cartesian definition into a radial-circumferential-like coordinate system. The boundary (i.e., in the circumferential direction) of the domain is discretised with finite elements, thus facilitating the computation of the angular variation of the unknown fields. The stress singularity along the radial direction emanating from the singular point is represented analytically. This automatically leads to accurate solutions

without local mesh refinement around the crack tip or other stress singularity points. Furthermore, no enrichment or analytical asymptotic expansion is required.

A definition of generalised stress intensity factors at a multi-material corner is proposed in Song et al. [51] based on the semi-analytical solution of singular stress fields obtained from the scaled boundary finite element method. It is consistent with the definitions of the classical stress intensity factors at crack tips and valid for all types of singularities. The generalised stress intensity factors can be determined directly from the scaled boundary finite element solution by following a standard stress recovery procedure. This method has also been extended to model piezoelectric materials [52, 53, 54]. The semi-analytical solution of stress field is convenient to use in the finite fracture mechanics [55]. Further improvements of the computed stress field can be achieved using error estimators such as the super-convergent patch recovery technique [56]. The fracture parameters, such as the stress intensity factors, T-stress and the coefficients of higher order terms are extracted directly based on their definitions [57, 12]. The scaled boundary finite element method can handle any configurations of multi-material corners. Since its inception, it has been applied to evaluate the free-edge stresses around holes in laminates [4], to compute the orders of singularity and stress intensity factors for multi-material plates under static loading and dynamic loading [58], and to predict the directions of cracks emerging from notches at bimaterial junctions [59]. Moreover, power-logarithmic singularities and the transition between the power and the power-logarithmic singularities can be represented by a stable algorithm [12]. These advantages are also preserved when applied to three-dimensional fracture problems. Recent published literature on the three-dimensional fracture analysis with the scaled boundary finite element method include homogeneous and interface cracks [60, 61, 62], composite laminates [63, 64, 65] and piezoelectric materials [66].

The scaled boundary finite element method only requires a subdomain (having the same role as an element in the finite element method) to satisfy the scaling requirement (i.e. the whole boundary is directly visible from a point) in the discretisation process. There is no restriction on the number of sides a subdomain can have. As a result, it can be formulated on polygonal elements of arbitrary number of edges, leading to a high degree of flexibility in mesh generation and remeshing. This feature, together with accurate semi-analytical solutions of stress singularities without local mesh refinement, greatly simplifies the simulation of crack propagation. A crack propagation modelling approach using the scaled boundary finite element method was first attempted by Yang [67] using large sized subdomains. The principles underlying the methodology have been extended to model nonlinear cohesive fracture in concrete [68, 69, 70, 71, 72] and dynamic fracture [73, 74].

The scaled boundary finite element method can be seamlessly coupled with the meshfree method [75, 76], the boundary element method [77, 78], the finite element method [79, 80, 81] and the extended finite element method [82, 83]. The principle underlying these approaches is to adopt the scaled boundary subdomains to discretise only the crack tips and the local regions in their vicinity. The remainder of the domain is discretised using the other methods of choice. When coupled with the finite element method, a simple remeshing algorithm that involves duplicating and readjusting the positions of nodes is applied to a background finite element mesh to propagate the crack. When coupled with the extended finite element method, level sets are used to update the crack trajectory. Complex crack propagation problems such as those in reinforced concrete [80] can be modelled.

Further improvements in terms of fully automating the modelling of crack propagation can be achieved using polygonal elements with arbitrary number of sides [84]. More recently, a hybrid approach which combines the use of polygon meshes with quadtree meshes proposed by Ooi et al. [85] further improves the computational efficiency of the scaled boundary finite element method for crack propagation modelling by exploiting the small number of patterns in the quadtree mesh.

This paper reviews the literature on the developments and the applications of the scaled boundary finite element method to linear elastic fracture mechanics. The paper is organised as follows: Section 2 presents an overview of the scaled boundary finite element method with particular emphasis on the concept of the scaled boundary finite element method when applied to linear elastic fracture mechanics problems. Section 3 briefly reviews the various approaches in which the scaled boundary finite element method is coupled with existing numerical methods in the literature with a focus on the more recent development that combines the extended finite element method and the scaled boundary finite element method. The application of the scaled boundary finite element method to stationary cracks and the accuracy of the method in determining the fracture parameters for various crack configurations, involving interface cracks, V-notches, etc. are presented in Section 4. Section 5 discusses the modelling strategy for crack propagation with a focus on the more recent developments that include the quadtree and polygonal meshes and also the combination with the extended finite element method. Examples of crack propagation are presented in Section 6. The major conclusions of the review are summarised in the last section.

2. Modelling of singular stress field by the scaled boundary finite element method

The theoretical formulation of the scaled boundary finite element method is detailed in Song and Wolf [49] and [86]. The applications to fracture analysis is covered in [51]. In this section, only key concepts of the scaled boundary finite element method are described.

2.1. Concept of scaled boundary finite element method

The construction of a polygonal element, referred to as a subdomain in the scaled boundary finite element method, is depicted in Fig. 1. The geometry of a subdomain must satisfy the scaling requirement, i.e. the whole boundary is directly visible from a point selected as the scaling centre O.

The boundary of the subdomain is divided into line elements (Fig. 1 with nodes shown as solid dots). The nodal coordinates are arranged in $\{x_b\}$, $\{y_b\}$. The geometry of an element is interpolated using the conventional finite element shape functions $[N(\eta)]$ formulated in the local coordinate η. The subdomain is described by scaling the boundary with the dimensionless radial coordinate ξ pointing from the scaling center O ($\xi = 0$) to a point on the boundary ($\xi = 1$). The scaling of the boundary with a value of $\xi < 1$ is shown in Fig. 1 by the thin line. A point (x, y) inside the domain is expressed, by scaling a point (x_b, y_b) on the boundary, as

$$x(\xi,\eta) = \xi x_b(\eta) = \xi [N(\eta)]\{x_b\} \tag{1a}$$

$$y(\xi,\eta) = \xi y_b(\eta) = \xi [N(\eta)]\{y_b\} \tag{1b}$$

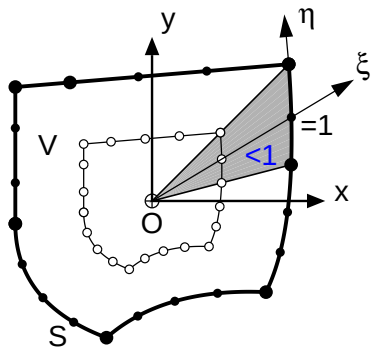

Figure 1: Scaled boundary finite element modeling of a polygonal subdomain

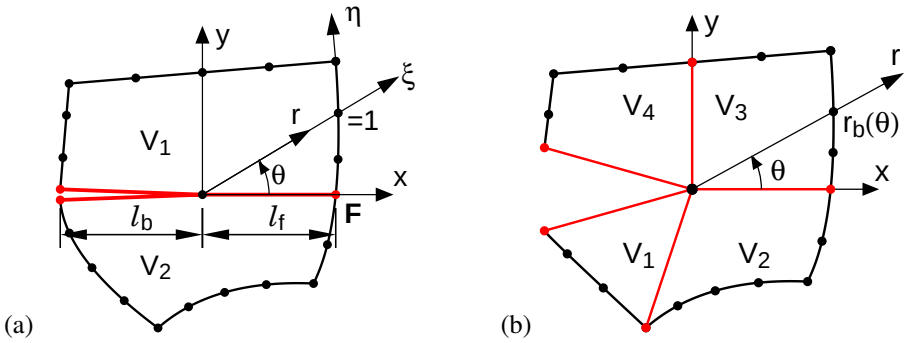

Figure 2: Modelling of stress fields around singularity points. The scaling center is chosen at a singularity point. (a) Interface crack. (b) Multi-material corner

The coordinates ξ, η are called the *scaled boundary coordinates*. The material in an area covered by scaling a boundary element (e.g. shaded area in Fig. 1) assumes the property of the element.

This approach is directly applicable to the modelling of singular stress fields. An interface crack and a multi-material wedge are shown in Fig. 2 as examples. Only the subdomains around the singularity points are considered. To model one subdomain, a scaling center O is selected at the singularity point. The part of boundary directly visible from the scaling center is discretised. For an ideal crack with zero thickness, two independent overlapping nodes (one for the upper crack face and the other for the lower crack face) are defined on the boundary. The crack faces and material interfaces are not discretised with any elements. They are represented by scaling the corresponding nodes on the boundary. This also implies that the crack faces and material interfaces must be straight lines. This requirement can always be satisfied to a given accuracy by applying the substructuring technique.

The scaled boundary coordinates in two dimensions resemble the polar coordinates r and θ. The polar coordinates

in Fig. 2 are expressed using Eq. (1) as

$$r(\xi,\eta) = \xi r_b(\eta) = \xi\sqrt{x_b^2(\eta)+y_b^2(\eta)} \tag{2a}$$

$$\theta(\eta) = \arctan\frac{y_b(\eta)}{x_b(\eta)} \tag{2b}$$

where $r_b(\eta)$ is the radial coordinate on the boundary. The angle θ depends on η only. As the whole boundary is visible from the scaling center, $\theta(\eta)$ is a single-valued function in its principal value ($-\pi < \theta \leq \pi$). The element number and the local coordinate η can be regarded as a discrete representation of the angle θ.

Along radial lines passing through the scaling center O and a node on the boundary, the nodal displacement functions $\{u(\xi)\}$ are introduced. The nodal displacements on the boundary follow as $\{u\} = \{u(\xi = 1)\}$. Isoparametric finite elements are used in the circumferential direction to interpolate the displacement functions piecewisely

$$\{u(\xi,\eta)\} = [N^u(\eta)]\{u(\xi)\} = [N_1(\eta)[I],\, N_2(\eta)[I], \ldots]\{u(\xi)\} \tag{3}$$

where $[I]$ is a 2×2 identity matrix. The stresses are expressed as (“,” denotes derivative)

$$\{\sigma(\xi,\eta)\} = [D]\left([B^1(\eta)]\{u(\xi)\}_{,\xi} + [B^2(\eta)]\{u(\xi)\}/\xi\right) \tag{4}$$

where $[B^1(\eta)]$ and $[B^2(\eta)]$ describe the strain-displacement relationship [49, 12].

After expressing the governing differential equations in the scaled boundary coordinates, Galerkin’s weighted residual method [49] or the principle of virtual work [87] can be applied in the circumferential direction η. The scaled boundary finite element equation in displacement is expressed as

$$[E^0]\xi^2\{u(\xi)\}_{,\xi\xi} + ([E^0] - [E^1] + [E^1]^T)\xi\{u(\xi)\}_{,\xi} - [E^2]\{u(\xi)\} = 0 \tag{5}$$

The coefficient matrices $[E^0]$, $[E^1]$ and $[E^2]$ are assembled from the element coefficient matrices [49], which are similar to the static stiffness matrices of 1D finite elements. The calculation and assemblage follow those in the standard finite element method.

The internal nodal forces along radial lines are equal to [49]

$$\{q(\xi)\} = [E^0]\xi\{u(\xi)\}_{,\xi} + [E^1]^T\{u(\xi)\} \tag{6}$$

2.2. Solution of displacements and stresses

The scaled boundary finite element equation in Eq. (5) is rewritten as a system of first-order ordinary differential equations

$$\xi\begin{Bmatrix} \{u(\xi)\} \\ \{q(\xi)\} \end{Bmatrix}_{,\xi} = -[Z]\begin{Bmatrix} \{u(\xi)\} \\ \{q(\xi)\} \end{Bmatrix} \tag{7}$$

with the Hamiltonian coefficient matrix

$$[Z] = \begin{bmatrix} [E^0]^{-1}[E^1]^T & -[E^0]^{-1} \\ -[E^2] + [E^1][E^0]^{-1}[E^1]^T & -[E^1][E^0]^{-1} \end{bmatrix} \tag{8}$$

which has pairs of eigenvalues λ_i and $-\lambda_i$. Equation (7) is decoupled by the block-diagonal Schur decomposition [88] of the matrix $[Z]$

$$[Z][\Psi] = [\Psi][S] \tag{9}$$

where $[\Psi]$ is a transformation matrix with independent column vectors. The matrix $[S]$ is block diagonal. Each of the diagonal blocks is in real Schur form (i.e., a quasi-upper triangular matrix consisting of 2×2 blocks on the diagonal, corresponding to complex conjugate eigenvalues, or 1×1 blocks, corresponding to real eigenvalues). The matrix $[S]$ is sorted in ascending order of the real parts of its eigenvalues (i.e. diagonal entries). The matrices $[S]$ and $[\Psi]$ are partitioned conformably into, respectively, $2N-1$ and $2N$ block matrices

$$[S] = \mathrm{diag}\left([S_1] \ \ldots [S_{N-1}] \begin{bmatrix} 0 & [I] \\ 0 & 0 \end{bmatrix} [S_{N+2}] \ \ldots \ [S_{2N}] \right) \tag{10}$$

$$[\Psi] = \begin{bmatrix} [\Psi_1^{(\mathrm{u})}] & \cdots & [\Psi_{N-1}^{(\mathrm{u})}] & [\Psi_N^{(\mathrm{u})}] & [\Psi_{N+1}^{(\mathrm{u})}] & [\Psi_{N+2}^{(\mathrm{u})}] & \cdots & [\Psi_{2N}^{(\mathrm{u})}] \\ [\Psi_1^{(\mathrm{q})}] & \cdots & [\Psi_{N-1}^{(\mathrm{q})}] & [\Psi_N^{(\mathrm{q})}] & [\Psi_{N+1}^{(\mathrm{q})}] & [\Psi_{N+2}^{(\mathrm{q})}] & \cdots & [\Psi_{2N}^{(\mathrm{q})}] \end{bmatrix} \tag{11}$$

The eigenvalues of the diagonal blocks of $[S]$ are disjoint and satisfy

$$\lambda([S_i]) = -\lambda([S_{2N+1-i}]) \tag{12}$$

It is worthwhile to note that the better known eigenvalue decomposition is a special case of the block-diagonal Schur decomposition where the size of all diagonal blocks is 1×1 (i.e., $[S_i]$ is a single eigenvalue and $[\Psi_i]$ is the corresponding eigenvector). The block-diagonal Schur decomposition is numerically robust, while the eigenvalue decomposition breaks down when a power-logarithmic singularity exists.

The solution satisfying the finiteness of displacements at the scaling center ($\xi = 0$) is expressed as

$$\{u(\xi)\} = \sum_{i=1}^{N-1} [\Psi_i^{(\mathrm{u})}] \xi^{-[S_i]} \{c_i\} + [\Psi_N^{(\mathrm{u})}] \{c_N\} \tag{13}$$

where $\{c_i\}$ are integration constants, and $[\Psi_N^{(\mathrm{u})}]$ represents the two modes of translational rigid body motion. Substituting Eq. (13) into Eq. (4) yields the stresses at a specified local coordinate η within a given element

$$\{\sigma(\xi,\eta)\} = \sum_{i=1}^{N-1} [\Psi_{\sigma i}(\eta)] \xi^{-[S_i]-[I]} \{c_i\} \tag{14}$$

where $[\Psi_{\sigma i}(\eta)]$ represents the stress modes corresponding to the displacement modes $[\Psi_i^{(\mathrm{u})}]$

$$[\Psi_{\sigma i}(\eta)] = [D] \left(-[B^1(\eta)][\Psi_i^{(\mathrm{u})}][S_i] + [B^2(\eta)][\Psi_i^{(\mathrm{u})}] \right) \tag{15}$$

The stress modes and the stresses are evaluated element-by-element at the Gauss points. For convenience in fracture analysis, the stress modes are transformed to polar coordinates r, θ (Fig. 2) using Eq. (2).

2.3. Definition and evaluation of generalised stress intensity factors

The solution of the stress field in Eq. (14) is a power series, similar to the asymptotic solution [1]. When the real parts of the eigenvalues of a diagonal block $[S_i]$ are between 0 and -1, the matrix power function $\xi^{-[S_i]-[I]}$ is

singular at $\xi = 0$. In the following, all such diagonal blocks are grouped into one block denoted as $[S^{(s)}]$ (superscript (s) for singular) and $-1 < \lambda([S^{(s)}]) < 0$ applies. The corresponding stress modes are denoted as $[\Psi^{(s)}]$. The integration constants are denoted as $\{c^{(s)}\}$. The singular stress field is separated from the solution in Eq. (14) and expressed as

$$\{\sigma^{(s)}(\xi,\eta)\} = [\Psi^{(s)}(\eta)]\xi^{-[S^{(s)}]-[I]}\{c^{(s)}\} \tag{16}$$

Introducing a characteristic length L, ξ is expressed in the polar coordinates r and θ (Eq. (2)) as

$$\xi = \frac{r}{r_b(\theta)} = \frac{L}{r_b(\theta)} \times \frac{r}{L} \tag{17}$$

where $r_b(\theta)$ is the distance from the scaling centre to the boundary along the radial line at angle θ (Fig. 2b). The matrix power function of ξ is rewritten in the polar coordinates as [51]

$$\xi^{-[S^{(s)}]-[I]} = \left(\frac{L}{r_b(\theta)}\right)^{-[S^{(s)}]-[I]} \left(\frac{r}{L}\right)^{-[S^{(s)}]-[I]} \tag{18}$$

To avoid proliferation of notations, the same function $\sigma^{(s)}$ is used to express singular stresses in polar coordinates. The singular stress field in Eq. (16) is expressed as

$$\{\sigma^{(s)}(r,\theta)\} = [\Psi_L^{(s)}(\theta)] \left(\frac{r}{L}\right)^{-[S^{(s)}]-[I]} \{c^{(s)}\} \tag{19}$$

where the stress modes at the characteristic length L are expressed as

$$[\Psi_L^{(s)}(\theta)] = [\Psi^{(s)}(\eta(\theta))] \left(\frac{L}{r_b(\theta)}\right)^{-[S^{(s)}]-[I]} \tag{20}$$

which is a linear transformation applied to the stress modes $[\Psi^{(s)}(\eta)]$ (for a given element, η and θ are related by a single-valued function in Eq. (2b)).

The case of two singular stress modes, i.e. $[S^{(s)}]$ is a 2×2 matrix, is considered. $\{c^{(s)}\}$ in Eq. (19) consists of two integration constants. Following the classical definition, two stress intensity factors are defined using the two stress components $\sigma_\theta^{(s)}(r,\theta)$ and $\tau_{r\theta}^{(s)}(r,\theta)$. Equation (19) still holds with the understanding that $\{\sigma^{(s)}(r,\theta)\} = [\sigma_\theta^{(s)}(r,\theta),\ \tau_{r\theta}^{(s)}(r,\theta)]^T$ applies and $[\Psi_L^{(s)}(\theta)]$ becomes a 2×2 matrix with only the entries corresponding to $\sigma_\theta^{(s)}(r,\theta)$ and $\tau_{r\theta}^{(s)}(r,\theta)$ retained. Equation (19) is further simplified by introducing a matrix of orders of singularity

$$[\tilde{S}^{(s)}(\theta)] = [\Psi_L^{(s)}(\theta)]([S^{(s)}] + [I])[\Psi_L^{(s)}(\theta)]^{-1} \tag{21}$$

Using Eq. (21), Eq. (19) is written as

$$\left\{ \begin{array}{c} \sigma_\theta^{(s)}(r,\theta) \\ \tau_{r\theta}^{(s)}(r,\theta) \end{array} \right\} = \left(\frac{r}{L}\right)^{-[\tilde{S}^{(s)}(\theta)]} [\Psi_L^{(s)}(\theta)]\{c^{(s)}\} \tag{22}$$

The generalised stress intensity factors $\{K(\theta)\} = [K_I(\theta),\ K_{II}(\theta)]^T$ at angle θ are defined in

$$\left\{ \begin{array}{c} \sigma_\theta^{(s)}(r,\theta) \\ \tau_{r\theta}^{(s)}(r,\theta) \end{array} \right\} = \frac{1}{\sqrt{2\pi L}} \left(\frac{r}{L}\right)^{-[\tilde{S}^{(s)}(\theta)]} \left\{ \begin{array}{c} K_I(\theta) \\ K_{II}(\theta) \end{array} \right\} \tag{23}$$

Comparing Eq. (23) to Eq. (22), the generalised stress intensity factors can be evaluated directly from the singular stress modes by

$$\left\{ \begin{array}{c} K_I(\theta) \\ K_{II}(\theta) \end{array} \right\} = \sqrt{2\pi L}[\Psi_L^{(\mathrm{s})}(\theta)]\{c^{(\mathrm{s})}\} \tag{24}$$

The generalised stress intensity factors can be easily evaluated by using Eq. (24) at any given angle θ, which is useful in determining the direction of crack propagation. The evaluation procedure is the same as the stress recovery procedures in standard finite elements. This technique is extended to define the stress and electric displacement intensity factors of cracks in piezoelectric materials [53]

It is shown in [51] that the definition in Eq. (23) includes the classical definitions of stress intensity factors as special cases. Since the solution of the singular stress field (Eq. (22)) has two integration constants, two generalised stress intensity factors are sufficient to fully define the singular stress field. It is customary to choose the stress intensity factors at angle $\theta = 0$. The generalised stress intensity factors $K_I = K_I(0)$ and $K_{II} = K_{II}(0)$ are defined by formulating Eq. (24) at $\theta = 0$

$$\left\{ \begin{array}{c} \sigma_\theta^{(\mathrm{s})}(r,0) \\ \tau_{r\theta}^{(\mathrm{s})}(r,0) \end{array} \right\} = \frac{1}{\sqrt{2\pi L}} \left(\frac{r}{L}\right)^{-[\tilde{S}^{(\mathrm{s})}(0)]} \left\{ \begin{array}{c} K_I \\ K_{II} \end{array} \right\} \tag{25}$$

The following two cases of classical definitions of the stress intensity factors are addressed:

1. *Crack in a homogeneous material*. The matrix of orders of singularity is equal to

$$[\tilde{S}^{(\mathrm{s})}(0)] = 0.5[I] \tag{26}$$

Substituting Eq. (26) into the definition of the generalised stress intensity factors in Eq. (25) leads the classical definition

$$\left\{ \begin{array}{c} \sigma_\theta^{(\mathrm{s})}(r,0) \\ \tau_{r\theta}^{(\mathrm{s})}(r,0) \end{array} \right\} = \frac{1}{\sqrt{2\pi L}} \left(\frac{r}{L}\right)^{-0.5} \left\{ \begin{array}{c} K_I \\ K_{II} \end{array} \right\} = \frac{1}{\sqrt{2\pi r}} \left\{ \begin{array}{c} K_I \\ K_{II} \end{array} \right\} \tag{27}$$

Note that the characteristic length L vanishes from the definition.

2. *Interficial crack between two isotropic materials*. The matrix of orders of singularity is

$$[\tilde{S}^{(\mathrm{s})}(0)] = \left[\begin{array}{cc} 0.5 & +\varepsilon \\ -\varepsilon & 0.5 \end{array} \right] \tag{28}$$

where ε is the oscillatory index [9]. Substituting Eq. (28) into the Eq. (25) results in the definition of the complex stress intensity factor $K_I + \mathrm{i}K_{II}$[9] expressed in vector form

$$\left\{ \begin{array}{c} \sigma_y^{(\mathrm{s})}(r,0) \\ \tau_{xy}^{(\mathrm{s})}(r,0) \end{array} \right\} = \frac{1}{\sqrt{2\pi r}} \left[\begin{array}{cc} \cos(\varepsilon \ln(r/L)) & -\sin(\varepsilon \ln(r/L)) \\ \sin(\varepsilon \ln(r/L)) & \cos(\varepsilon \ln(r/L)) \end{array} \right] \left\{ \begin{array}{c} K_I \\ K_{II} \end{array} \right\}$$

The magnitude of the complex stress intensity factor $\sqrt{K_I^2 + K_{II}^2}$ is independent of the characteristic length L.

The above procedure can be used to determine the $T-$stress by extracting the terms with $\lambda([S]) = -1$ [12].

3. Coupling with other partition of unity methods

The accuracy of the scaled boundary finite element method to model the stress field in the vicinity of singularities has also inspired coupled methods that combines it with other numerical approaches such as the finite element method [79, 81], the boundary element method [77, 78], the extended finite element method [82, 83] and the element-free Galerkin method [76]. These coupled approaches facilitate the treatment of the singularity in the vicinity of a crack tip using the scaled boundary finite element method in combination with the ease of treating complex boundaries.

The introduction of the extended finite element method [36, 40, 38], based on the partition of unity framework, has revolutionised the way the singularities and other discontinuities are modelled. The salient feature is that the internal discontinuities could be modelled independent of the underlying finite element mesh and the mesh need not be updated when the crack propagates. Built on the finite element framework, the method relies on augmenting the conventional finite element approximation basis with *a priori* known functions (analytical or numerical) that capture the local behaviour. Although robust, it leads to other related difficulties, such as blending problems, numerical integration of enrichment functions, ill-conditioning of the resulting stiffness matrix and an enlarged system of equations to solve [38, 89, 90]. Moreover, depending on the problem description, new enrichment functions are required for example, for orthotropic materials, functionally graded materials, cracks terminating at the interface and bi-material interface cracks. Another major hurdle is the computation of the fracture parameters such as the stress intensity factors and $T-$ stress, which requires specialized techniques such as path-independent integrals [23, 22].

Natarajan and Song [91] introduced the extended scaled boundary finite element method, wherein the scaled boundary finite element method was combined with the extended finite element method. Li et al., [83] further extended the work by combining the extended scaled boundary finite element method with level set method to simulate crack propagation. Egger et al., [56] proposed a blocked Hamiltonian Schur decomposition for the solution process of the extended scaled boundary finite element method and compared the performance of the method with the conventional finite element method and the extended finite element method. It was observed that it yields super-convergence in estimating the stress intensity factors. Within this framework, as opposed to enriching a small region in the vicinity of the crack tip with asymptotic functions in the extended finite element method, the region is modelled as a scaled boundary subdomain. The region behind the crack tip is modelled using the extended finite element framework and the rest of the region is treated as in the conventional finite element method. This alleviates the requirement of: (a) *a priori* knowledge of asymptotic expansions of the displacements and/or stress fields and (b) special numerical integration. Moreover, the approach can be combined with any existing (extended) finite element code and the fracture parameters could be estimated from the definition of the generalized stress intensity factors (c.f. 2.3).

This approach leads to different non-overlapping regions ($\Omega = \Omega^{\text{fem}} \cup \Omega^{\text{xfem}} \cup \Omega^{\text{sbfem}}$) (see Fig. 3). The different regions are identified as:

- Ω^{fem}- Standard elements - contains a set of elements that are not intersected by the cracks. Within this region, the conventional finite element approximation is employed to represent the smooth behavior.

- Ω^{xfem}- Enriched elements - list of elements that are completely cut by the crack (known as split element in the

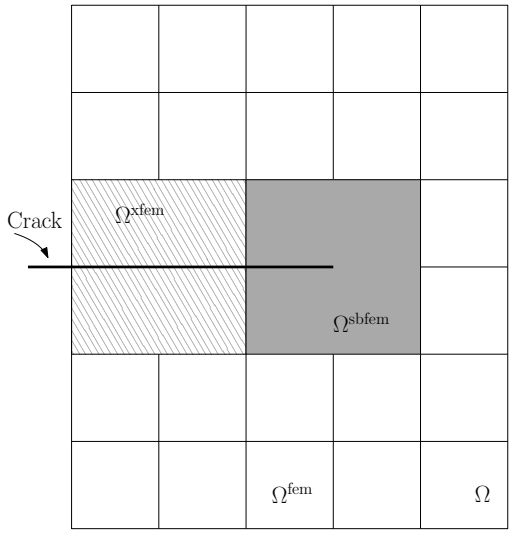

Figure 3: A representative finite element mesh with an embedded crack (solid black line). The various regions of partition of unit are identified. In this descriptive figure, one layer of FE is replaced with the scaled boundary region.

extended finite element terminology). Their nodal support is enriched with Heaviside function to represent the discontinuity across the crack surface.

- Ω^{sbfem}- Scaled boundary finite element region - set of elements that define the scaled boundary finite element domain. The asymptotic stress field in the vicinity of the crack tip is represented semi-analytically

As different approximation functions are used in different regions, a coupling scheme is devised in [91, 83], eliminating the displacement incompatibility in the coupled region. This is achieved using a transition matrix $[T]$ to match the nodal displacements along the boundary in the coupling region. For the nodes that are on the boundary of Ω^{fem} and Ω^{sbfem}, no special treatment is required[1]. For the nodes that are shared by Ω^{fem} and Ω^{xfem}, the procedure similar to that of the extended finite element framework is employed. The region that is shared by Ω^{sbfem} and Ω^{xfem} requires special treatment. In the scaled boundary finite element method, the crack is modelled as an open domain (see Fig. 4) while it is represented by a Heaviside function in case of the extended finite element method. The augmentation of a Heaviside function introduces additional degrees of freedom that account for the jump in the displacement across the crack surface.

The displacement approximations for the extended finite element method and the scaled boundary finite element method are given by:

$$\{u(x,y)\} = \begin{cases} [N^{fe}(x,y)]\{q\} + [N^{fe}(x,y)][H(x,y)]\{a\} & (x,y) \in \Omega^{\text{fem}} \cup \Omega^{\text{xfem}} \\ [N^{u}(\eta)]\{u(\xi)\} & (x,y) = (x(\xi,\eta), y(\xi,\eta)) \in \Omega^{\text{sbfem}} \end{cases} \tag{29}$$

As the displacements are required to be compatible, the displacements from the extended finite element method domain are matched to the displacements from the scaled boundary finite element method domain through the transformation

[1]This is because the scaled boundary finite element method employs finite element approximation basis on the boundary, and hence the unknown coefficients from the scaled boundary finite element method and the finite element method are compatible.

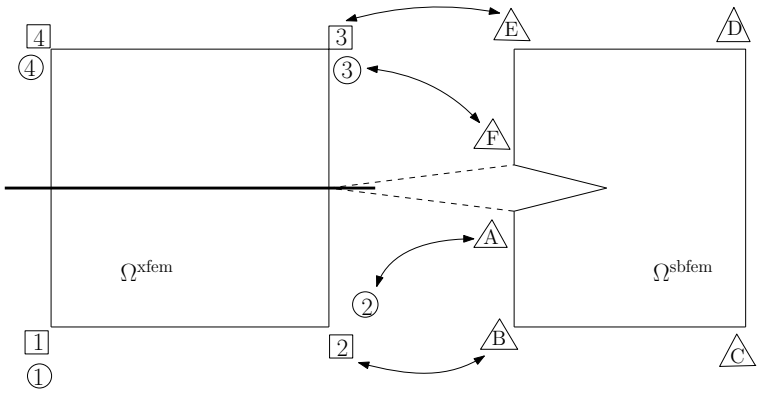

Figure 4: The coupling of the extended finite element region with the scaled boundary finite element region. 'Circled' nodes are enriched with the Heaviside function and 'Solid' line represents the crack.

matrix $[T]$. For the elements shown in Fig. 4, the displacements from the extended finite element method and the scaled boundary finite element method are matched by:

$$\underbrace{\begin{Bmatrix} \{u_B\} \\ \{u_E\} \\ \{u_A\} \\ \{u_F\} \end{Bmatrix}}_{\{u^2_{bK}\}} = \underbrace{\begin{bmatrix} [I] & 0 & 0 & 0 \\ 0 & [I] & 0 & 0 \\ N_2^{fe}(x_A,y_A)[I] & N_3^{fe}(x_A,y_A)[I] & 0 & -2N_3^{fe}(x_A,y_A)[I] \\ N_2^{fe}(x_F,y_F)[I] & N_3^{fe}(x_F,y_F)[I] & 2N_2^{fe}(x_F,y_F)[I] & 0 \end{bmatrix}}_{[T]} \underbrace{\begin{Bmatrix} \{q_2\} \\ \{q_3\} \\ \{a_2\} \\ \{a_3\} \end{Bmatrix}}_{\{u^2_{xF}\}} \tag{30}$$

where $[I]$ is the identify matrix and $[T]$ is the transformation matrix that relates the displacements on the interface between Ω^{sbfem} and Ω^{xfem}. To ensure the compatibility of the displacements and to assemble the stiffness matrix to the global stiffness matrix, the stiffness matrix in Ω^{sbfem} and the force vector are rearranged as:

$$\begin{bmatrix} [K_{aa}] & [K_{ab}] \\ [K_{ba}] & [K_{bb}] \end{bmatrix} \begin{Bmatrix} \{u^1_{bK}\} \\ \{u^2_{bK}\} \end{Bmatrix} = \begin{Bmatrix} \{f_a\} \\ \{f_b\} \end{Bmatrix} \tag{31}$$

where $[K_{aa}]$, $\{u^1_{bK}\}$ and $\{f_a\}$ correspond to the stiffness matrix, the displacement vector and the force vector for the nodes that are not shared with the element that is completely cut by the discontinuity surface in the Ω^{xfem}, $[K_{bb}]$, $\{u^2_{bK}\}$ and $\{f_b\}$ are the stiffness matrix, the displacement vector and the force vector that are shared with the element that is completely cut by the discontinuity surface and $[K_{ab}]$ and $[K_{ba}]$ are the coupling matrices. Now, applying the transformation matrix, results in

$$\begin{bmatrix} [K_{aa}] & [K_{ab}][T] \\ [T]^T[K_{ba}] & [T]^T[K_{bb}][T] \end{bmatrix} \begin{Bmatrix} \{u_{qS}\} \\ \{u_{xF}\} \end{Bmatrix} = \begin{Bmatrix} \{f_a\} \\ [T]^T\{f_b\} \end{Bmatrix} \tag{32}$$

The transformation matrix $[T]$ requires only the evaluation of the shape functions at the crack mouth. The assembly procedure follows that of the conventional finite elements. The resulting global stiffness matrix retains a similar structure to that of the conventional finite element method.

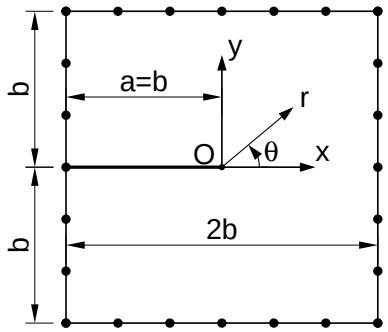

Figure 5: Edge-cracked square body: Geometry and boundary discretisation with 8 cubic elements.

4. Examples of evaluation of stress intensity factors and $T-$stress

Since its inception, the scaled boundary finite element method has been applied to compute not only the stress intensity factors, but also T-stress and higher order terms in the vicinity of a singularity e.g. a crack or a notch. The robustness of the scaled boundary finite element method for such applications has been reported in the literature for two-dimensional analyses of problems ranging from linear elastic materials [92, 93, 94, 95], laminated composites [96], piezoelectric materials [97, 52, 98, 53, 54] and elastomers [99]. Applications in three dimensions have also been reported [64, 60, 100, 61, 62].

In this section, several examples are presented to demonstrate the application of the scaled boundary finite element method, including one example from the extended finite element method, in evaluating the stress intensity factors and $T-$stress. Interested readers may refer to Chowdhury et al. [101] for highly accurate results of the stress intensity factors and $T-$stress for several standard specimens. Examples of dynamic stress intensity factors and $T-$stress are presented in [102].

4.1. Edge-cracked homogeneous square body

An edge-crack square body under plane strain condition is shown in Fig. 5. The size of the square is $2b$. The length of the crack is $a = b$. The material is isotropic with Young's modulus E and Poisson's ratio $\nu = 0.25$. The boundary condition is prescribed according to the asymptotic solution of stresses in such a way that $K_I/(p\sqrt{a}) = 1$, $K_{II}/(p\sqrt{a}) = 1$ and $T/(K_I/\sqrt{a}) = 1$ apply (p is a constant with the unit of stress).

The square boundary is discretised with cubic (4-node) elements. To perform a convergence study, five meshes with 8, 16, 24, 32 and 48 elements are used. The nodes are evenly spaced along the edges. The mesh with 8 elements is shown in Fig. 5.

The stress intensity factors K_I, K_{II} and $T-$stress are determined. The results are normalised and shown in Table 1. The error of the results obtained with the coarsest mesh (8 elements) is less than 1%. When 48 cubic elements are used, the results are accurate up to the first 6 significant digits. The relative errors are plotted versus the number of degrees of freedom (which is inversely proportional to the element length) in Fig. 6a. The slopes of the convergence curves are approximately equal to -4, showing a super-convergent rate.

Table 1: Normalised stress intensity factors K_I, K_{II} and $T-$stress of edge-cracked square body

	Number of Elements					Exact
	8	16	24	32	48	
$K_I/(p\sqrt{a})$	1.004415	1.000011	0.999994	0.999997	0.999999	1
$K_{II}/(p\sqrt{a})$	1.007734	1.000835	1.000181	1.000060	1.000009	1
$T/(K_I/\sqrt{a})$	1.005591	1.000208	1.000034	1.000010	1.000002	1

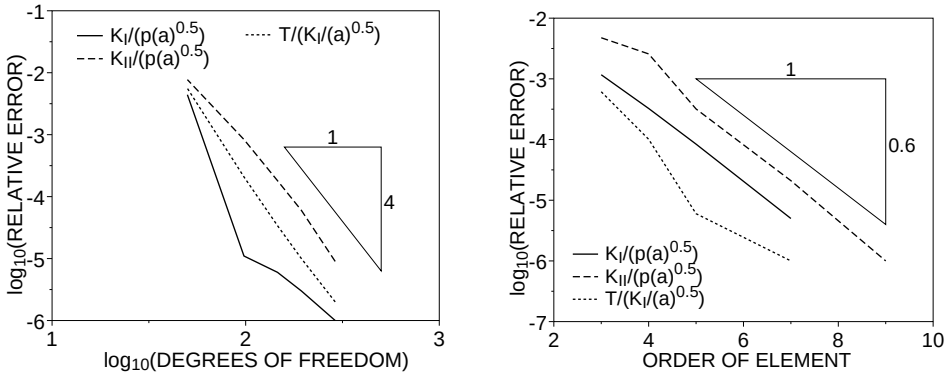

(a) $h-$refinement (b) $p-$refinement

Figure 6: Convergence of stress intensity factors and $T-$stress of edge-cracked square body

The convergence with increasing element order is also examined. The boundary is divided into 8 spectral elements of the same length. The element orders are 4, 6, 8 to 10. A semi-log plot of the errors in the results of the stress intensity factors K_I, K_{II} and $T-$stress versus the element order is shown in Fig. 6b. Exponential convergence is observed.

4.2. Interface central crack between two anisotropic materials

A rectangular body composed of two orthotropic materials is shown in Fig. 7a. The height and width of the rectangle are $2H$ and $W = H$, respectively. A central crack of length $2a = 0.4W$ is located on the material interface. The elastic properties are $E_{11} = 100$ GPa, $E_{22} = 50$ GPa, $G_{12} = 50.35426$ GPa and $\nu_{12} = 0.3$ for Material 1 and $E_{11} = 100$ GPa, $E_{22} = 10$ GPa, $G_{12} = 27.034099$ GPa and $\nu_{12} = 0.3$ for Material 2. Plane stress conditions are assumed. The characteristic length is chosen as $L = 2a$.

The rectangular body is divided into 4 subdomains as shown in Fig. 7b. The scaling centres of the subdomains are indicated by the markers "$\oplus$". The crack tips are at the scaling centres of subdomains 1 and 2. The boundary visible from the scaling centres are discretised with 10-th order spectral elements. The matrix of orders of singularity obtained from the present analysis, denoted as $[\tilde{S}^{(s)}]_{\text{present}}$, and from the analytical solution [11], denoted as $[\tilde{S}^{(s)}]_{\text{exact}}$, are equal to

$$[\tilde{S}^{(s)}]_{\text{present}} = \begin{bmatrix} 0.500001 & -0.044840 \\ 0.110382 & 0.499999 \end{bmatrix}; \qquad [\tilde{S}^{(s)}]_{\text{exat}} = \begin{bmatrix} 0.500000 & -0.044839 \\ 0.110383 & 0.500000 \end{bmatrix}$$

The two results agree with each other up to the first 5 significant digits. The generalised stress intensity factors are

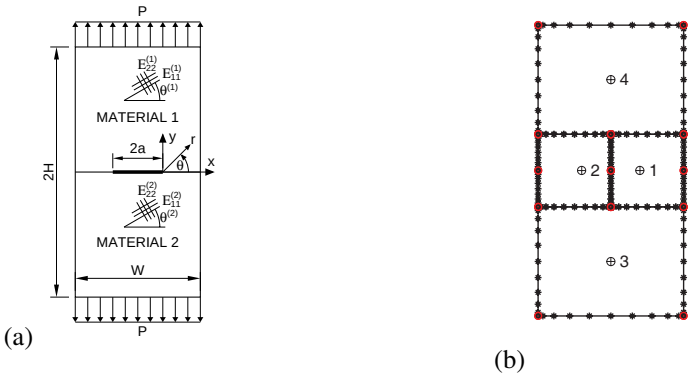

Figure 7: Interface central crack between two anisotropic materials. (a) Geometry. (b) Mesh.

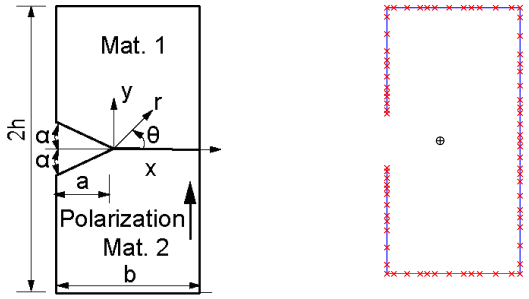

(a) Geometry (b) Scaled boundary finite element mesh

Figure 8: Bimaterial interface notch subjected to uniform temperature change

obtained as $K_I = 1.12P\sqrt{\pi a}$, $K_{II} = -0.257P\sqrt{\pi a}$. They are converted to the stress intensity factors defined in Cho et al. [11] as $\sqrt{K_1^2+K_2^2} = 1.776P\sqrt{\pi a}$ and $K_2/K_1 = -0.146$, which agree well with $\sqrt{K_1^2+K_2^2} = 1.772P\sqrt{\pi a}$ and $K_2/K_1 = -0.143$ reported in Cho et al. [Table 3, 11].

4.3. Piezoelectric bimaterial with an interface edge notch subjected to temperature change

A V-notched piezoelectric bimaterial body is shown in Fig. 8a with $a = 0.4b$ and $h = b$. The opening angle of the notch is equal to 2α. Material 1 is piezoelectric cadmium selenide and material 2 is PZT-6B. The material constants are given in [53]. The uniform temperature change is T_0. The scaled boundary finite element mesh of 5-node (4th-order) elements is shown in Fig. 8b. The characteristic length is chosen as $L = 2a$.

The interface edge crack ($\alpha = 0$) is considered. The stress and electric displacement intensity factors of the crack tip are evaluated at $\theta = 0^\circ$. The results of normalised stress and electric displacement intensity factors ($K_I/(p_{33}^1 T_0\sqrt{\pi a})$, $K_{II}/(p_{33}^1 T_0\sqrt{\pi a})$ and $K_{IV}/(\beta_3^1 T_0\sqrt{\pi a})$), where the superscript "1" in p_{33} and β_3 represents material 1, are listed in Table 2 for increasing element order. It is observed that the results obtained using 10-th order elements converge to the first five significant digits. The converged orders of singularity are λ =0.5, 0.5±0.0197i.

Table 2: Normalised intensity factors of an interface edge crack in cadmium selenide/PZT-6B

Element order	4	6	8	10	14
$K_I/(p_{33}^1 T_0\sqrt{\pi a})$	6.8563E-4	7.1596E-4	7.0537E-4	7.0537E-4	7.0537E-4
$K_{II}/(p_{33}^1 T_0\sqrt{\pi a})$	5.2955E-2	5.2900E-2	5.2898E-2	5.2897E-2	5.2897E-2
$K_{IV}/(\beta_3^1 T_0\sqrt{\pi a})$	7.6679E-2	7.6679E-2	7.6181E-2	7.6156E-2	7.6156E-2

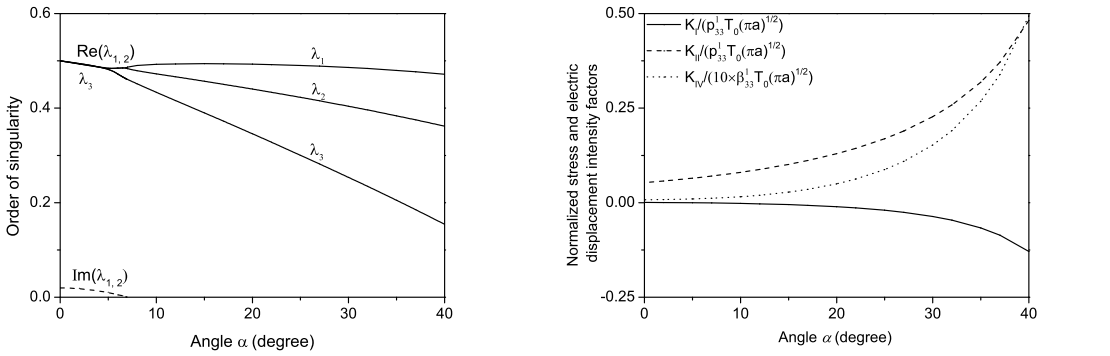

(a) Order of singularity

(b) Normalised stress and electric displacement intensity factors

Figure 9: Interface edge notch in cadmium selenide/PZT-6B with varying opening angle α

The change in the stress intensity factors with varying notch opening angle α is investigated. The orders of singularity are shown in Fig. 9a when varying the opening angle. A real order λ_3 and the real part $\mathrm{Re}(\lambda_{1,2})$ of a pair of complex conjugate eigenvalues decrease when α varies from 0° to around 6.9°. As α increases further, three real orders of singularity exist. Two real orders of singularity λ_1 and λ_2 separate as α increases further. The stress and electric displacement intensity factors are shown in Fig. 9b. It is observed that K_{II} and K_{IV} increase as the interface notch becomes wider, whereas K_I decreases.

4.4. Interface edge crack between two isotropic materials subjected to tension

A bimaterial body with an edge crack $(a/L = 0.5)$ subjected to uniform tension $(p = 1)$ is considered (see Fig. 10). The material is assumed to be isotropic with Young's modulus, $E_1 = 1$ and $E_1/E_2 = 2$ and Poisson's ratio $\nu_1 = \nu_2 = 0.3$. Note that consistent units are used in this example. A state of plane strain is considered. This problem is solved by employing the extended scaled boundary finite element method. The discontinuities (both the crack and the material interface) are represented independent of the underlying finite element mesh. The material interface that does not contain the crack is treated within the extended finite element framework. A small region in the vicinity of the crack tip is replaced with the scaled boundary domain, which is identified by:

- Selecting the nodes whose nodal support is intersected by the discontinuous surface, viz., crack or the material interface.

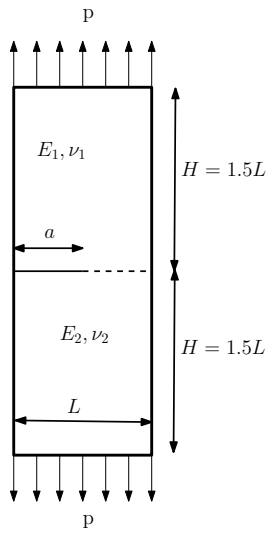

Figure 10: Interface edge crack between two isotropic materials subjected to far field tension: geometry and boundary conditions.

Table 3: Convergence of the mode I and mode II stress intensity factors for an interface edge crack in tension. The results are normalised with the stress intensity factors reported in [103].

Number of layers	Normalized stress intensity factors	
	K_I	K_{II}
3	0.98209	1.01866
4	1.00319	1.01007
5	1.00103	1.00037
6	1.00043	0.99776
7	0.99968	0.99664
8	0.99929	0.99963

- The elements containing these nodes are selected and only the information on the boundary of this set of elements is retained. The degrees of freedom of the nodes within the domain are condensed during the solution process.

Within this region, i.e, Ω^{sbfem}, the scaled boundary formulation is employed to compute the stiffness matrix. Note that no special numerical integration technique is required. Figure 11 shows a typical finite element mesh used for this study. The scaled boundary region Ω^{sbfem} is indicated by $A-B-C-D$. In this example, the interface aligns with the element edge. To represent the jump across the crack face, the 'circled' nodes are enriched with the Heaviside function. The crack is aligned to the bimaterial interface and a structured quadrilateral mesh is used for the spatial discretisation.

The influence of the number of layers on the numerical stress intensity factors is demonstrated in Table 3 for a

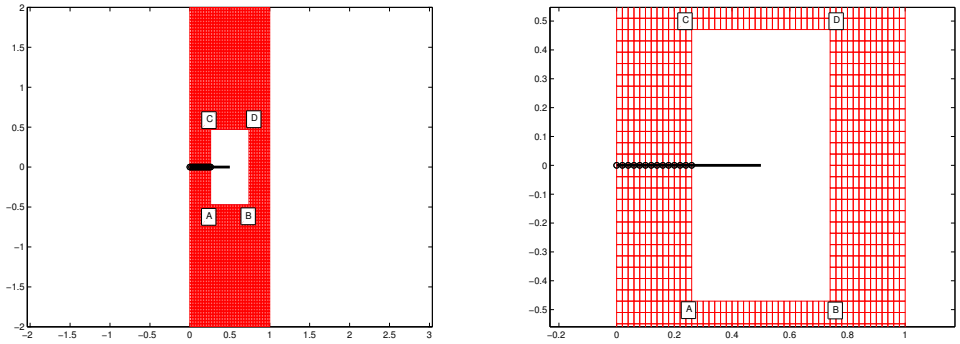

Figure 11: A typical discretization for a bimaterial interface crack.

structured mesh of 51 $\times$ 102 quadrilateral elements. It is inferred that the results from the extended scaled boundary method converge and are close to the solution reported in the literature [103]. From this study, it can be concluded that for a given mesh, 4-5 layers of elements if replaced with the scaled boundary finite element domain yields reasonably accurate solutions.

5. Modelling of crack propagation

The scaled boundary finite element method allows a problem domain to be discretised into polygons with arbitrary number of sides. This feature is very convenient for applications that involve continuous change in the problem geometry such as crack propagation. The changes in the mesh instigated by crack growth can be easily accommodated using simple yet efficient remeshing algorithms or level sets. Since the scaled boundary finite element method is accurate in modelling the singular stress fields in the vicinity of crack tips, these approaches eliminate the need for fine crack tip meshes and result in robust techniques for crack propagation analyses. This section reviews the more recent developments of the scaled boundary finite element method-based approaches for crack propagation modelling and presents several of their applications in various fields in fracture mechanics.

5.1. Extended scaled boundary finite element method

The extended finite element method facilitates the use of structured quadrilateral meshes. The geometric discontinuities are represented independent of the underlying mesh topology using level sets and the local behaviour is captured through the augmented asymptotic functions. In the conventional extended finite element method, as the crack propagates, new set of nodes whose nodal support is intersected by the discontinuity are identified. The approximation functions of these nodes are then augmented with appropriate functions. In the extended scaled boundary finite element method, as the crack propagates, new set of nodes are identified. However, instead of enriching the approximation basis, the crack tip region is modelled as a scaled boundary finite element subdomain and appropriate level set functions are added to the mesh to model the crack geometry. Figure 12 shows a representative crack path and its propagation. For more details, interested readers are referred to the recent work of Li et al. [83].

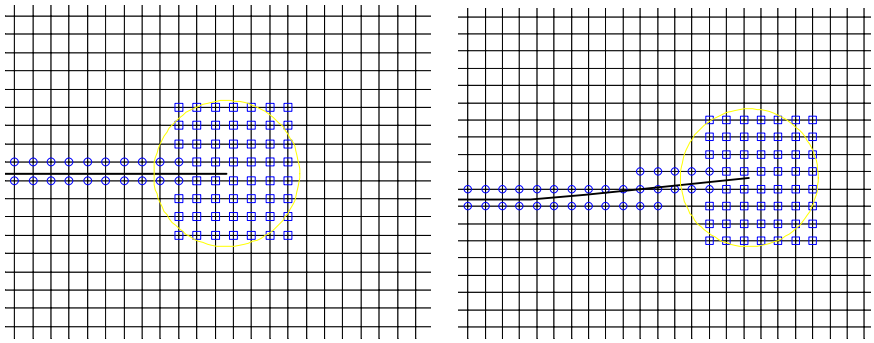

Figure 12: Representative crack path and its trajectory. 'Circled' nodes are treated within the extended finite element framework and the nodes marked with 'squares' are represented by the scaled boundary domain. Note that only the boundary nodes are considered and the degrees of freedom on the interior nodes are condensed during the solution process.

The coupling of the scaled boundary finite element method with the extended finite element method enables crack propagation to be modelled without remeshing. At the same time, it preserves the accuracy of the computed stress intensity factors without the need of special integration techniques in the region around the crack tip as would be required in an approach that is purely based on the extended finite element method.

5.2. Polygon meshes

A methodology for modelling crack propagation using polygonal meshes was developed by Ooi et al. [104]. Polygonal meshes are generated from Voronoi diagrams [105] or from a Delaunay triangulated mesh [104, 106]. The resulting polygon mesh automatically satisfies the scaling requirement. The polygon containing the crack tip is called a "*crack polygon*". To ensure the accuracy of solution of the singular stress field, an edge of the cracked polygon is discretised with multiple line elements. In order to model the crack propagation process, two different polygonal-based remeshing algorithms have been proposed by Ooi et al. [104] and Shi et al. [107], Ooi et al. [108].

The algorithm developed by Shi et al. [107] and Ooi et al. [108] involves the local remeshing of a small area in the vicinity of the crack tip. It is robust and ensures the generation of high-quality polygon meshes. The remeshing algorithm is depicted in Fig. 13 for one crack propagation step. The background triangular mesh used to generate the polygon mesh is also drawn in the figure. The triangles cut by the crack increment are first identified (enclosed by the thick solid lines in Fig. 13b and Fig. 13c). A patch is constructed by adding one layer of triangular elements connected to the cut ones (indicated by the thick dotted lines in Fig. 13b and Fig. 13c). The triangular elements inside the patch are removed (Fig. 13d) and a Delaunay triangulation is performed on the empty patch considering the presence of the crack (Fig. 13e). A local polygon mesh, as shown in Fig. 13f, can then be generated from the new triangular mesh following the procedures described in [104]. As the remeshing involves only a small patch of polygons around the crack tip at each crack propagation step, it results in a minimal amount of change to the global mesh structure.

The use of polygon meshes provides appealing alternative approaches for model problems in engineering involving crack propagation. Many aspects of crack propagation have been explored using these approaches e.g. nonlinear crack propagation in concrete [84, 107], elasto-dynamic crack propagation [108] and functionally graded materials [109].

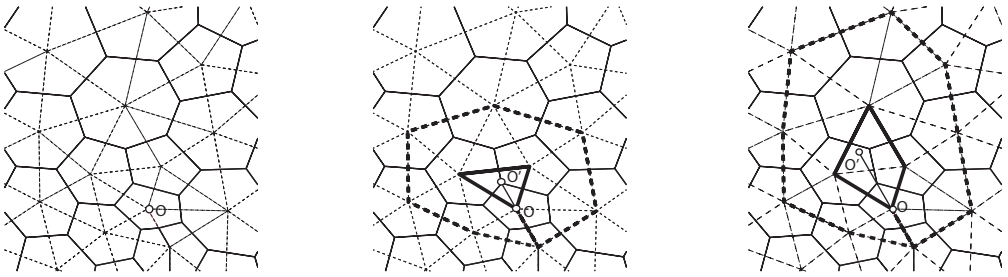

(a) Current mesh around crack tip

(b) Patch for local remeshing for crack increment (Case 1)

(c) Patch for local remeshing for crack increment(Case 2)

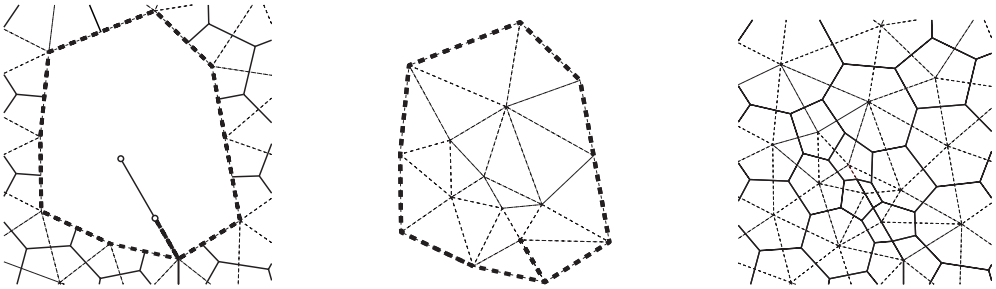

(d) Removal of background cells in the patch

(e) Local remeshing of the patch

(f) Polygon mesh incorporating crack increment

Figure 13: Local remeshing algorithm of polygonal mesh

5.3. Hybrid quadtree-polygon meshes

The scaled boundary finite element method is highly complementary with quadtree meshes owing to the flexibility in the shapes of the subdomain. A quadtree algorithm involves recursive division of each parent cell into four children until the resolution is fine enough (see Fig. 14a for an example). It is particularly efficient for data storage and retrieval. In computational mechanics, the direct use of quadtree meshes is hindered by the existence of hanging nodes (Fig. 14a). The quadtree decomposition is usually employed in finite element mesh generation algorithms for its efficiency and followed by the triangulation of quadtree cells. Since the scaled boundary finite element method can directly model a quadtree cell as an arbitrary-sided polygon, the triangulation process is eliminated.

To derive the most efficiency from quadtree meshes, it is useful to use balanced quadtree meshes [110] in which the sizes of the adjacent cells differ at most by a factor of 2. In a balanced quadtree mesh, the patterns of the cells depend on the existence of the midpoint nodes (Fig. 14b, where the locations of possible midpoint nodes are indicated by solid dots). The total number of unique cell patterns is equal to $2^4 = 16$. These are referred to as the "*master cells*". All the other cells can be obtained by scaling one of the master cells. In an analysis, only the stiffness (and mass) matrices of these 16 cells need to be computed for a given material. These are stored for quick data retrieval and scaling according to the size of the actual cells [85]. For isotropic materials, the unique patterns are reduced to 6 by considering rotation.

Some of the square quadtree cells are trimmed by the crack path and the boundary of the problem domain (Fig. 15).

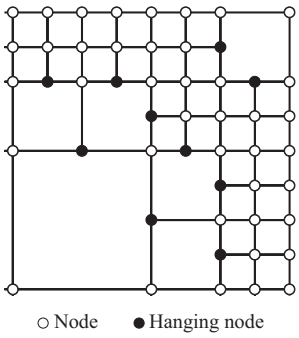

(a) A balanced quadtree mesh

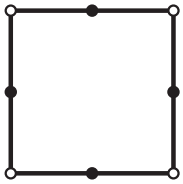

(b) A balanced quadtree cell.

Figure 14: Example of quadtree mesh generation

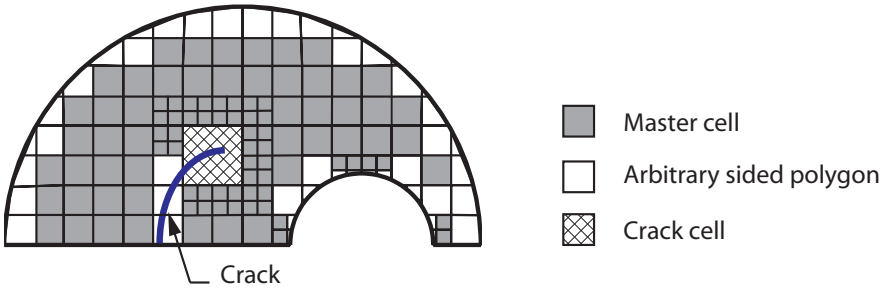

Figure 15: Generic hybrid polygon-quadtree mesh.

These trimmed cells are polygons and can also be directly modelled as scaled boundary subdomains. The region enclosing the crack tip is modelled as a crack polygon. The mesh consisting of a mixture of square and polygonal subdomains is referred to as a hybrid quadtree-polygon mesh [85]. Typically, the bulk of the mesh consists of the square cells that can be scaled from master cells. During the simulations, only the stiffness matrices from the arbitrary sided polygons need to be computed. This approach increases the computational efficiency in simulations that require repetitive computation of stiffness and/or mass matrices such as that in crack propagation.

The remeshing process during crack propagation is depicted in Fig. 16. The current mesh around the crack tip is shown in Fig. 16a. The crack increment and the radius of a circle Ω_{cir} controlling the size of the crack polygon are given as inputs. A balanced quadtree mesh is created around the new crack tip (Fig. 16b). The size of the quadtree cells is chosen in a way that there are sufficient nodes on the boundary of the cracked polygon for accurate computation of the singular stress field around the new crack tip. The crack polygon is created by merging the cells that overlap Ω_{cir} into a single crack polygon. Each of the cells cut by the crack path are then split into two leading to the mesh in Fig. 16c.

Applications of the hybrid quadtree-polygon approach for crack propagation modelling has been reported for several fields in fracture mechanics including nonlinear cohesive fracture [111] and elasto-dynamic fracture [112]. For

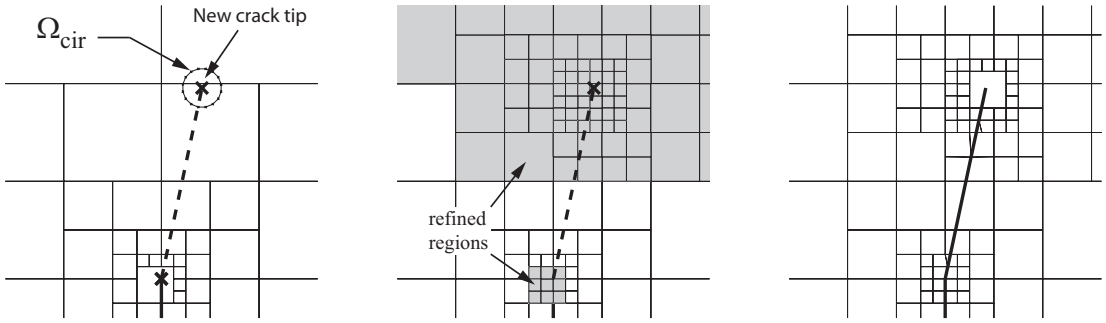

(a) Mesh around the crack tip and the crack increment

(b) Remesh around the new crack tip

(c) Generation of the new crack polygon

Figure 16: Remeshing algorithm using polygonal meshes via local remeshing.

such types of problems which involve repetitive computations of the stiffness and mass matrices, the use of hybrid quadtree-polygon meshes was capable of limiting the time required to compute these variables to only 9.5% of the total CPU time over the entire simulation [112].

6. Examples of crack propagation

This section presents several examples of applications of the scaled boundary finite element method for crack propagation modelling. The examples are intended to cover a broad range of applications including quasi-static fracture, dynamic fracture, fatigue fracture, cracks at the interface or terminating at the interface and cracks in heterogeneous materials. The application of the scaled boundary finite element method using polygonal meshes, the hybrid-polygon-quadtree meshes and the extended scaled boundary finite element method will be presented. The first example demonstrates the efficacy of the extended scaled boundary finite element method, wherein a structured quadrilateral mesh is adopted. The next two examples employ the scaled boundary finite element method with adaptive quadtree decomposition and the last two examples demonstrates the applicability of handling discontinuities with arbitrary sided polygons. The results from the scaled boundary finite element method are compared with the finite element solution.

The crack growth direction is determined by the maximum hoop stress criterion, which states that the crack will propagate from its tip in the direction θ_c where the circumferential stress $\sigma_{\theta\theta}$ is maximum. The critical angle is computed by solving the following equation:

$$K_I \sin\theta_c + K_{II}(3\cos\theta_c - 1) = 0 \tag{33}$$

Solving the above equation, gives the crack propagation angle:

$$\theta_c = 2\arctan\left[\frac{-2\left(\frac{K_{II}}{K_I}\right)}{1+\sqrt{1+8\left(\frac{K_{II}}{K_I}\right)^2}}\right] \tag{34}$$

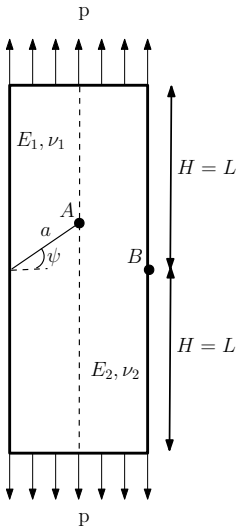

Figure 17: Geometry and boundary conditions for a crack terminating at the material interface. The thick solid line represents the crack and is assumed to be in material 2 with Young's modulus E_2 and Poisson's ratio ν_2 and terminating at the interface between material 1 and 2. The angle of the crack is ψ.

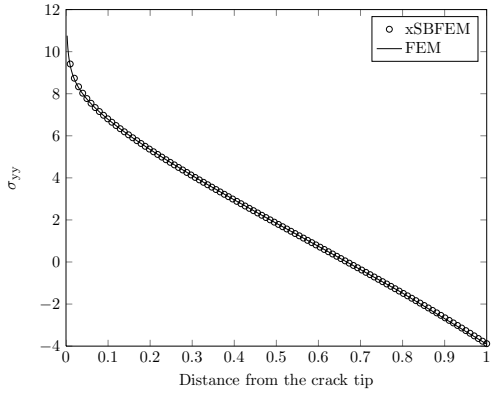

Figure 18: Stress along the loading direction (see Fig. 17) ahead of the crack tip. The present result (xSBFEM) is compared with a fine finite element model that employs quarter point elements to represent the singular stress field (FEM).

6.1. Propagation of a crack terminating at an interface

A crack terminating at the bimaterial interface of a bimaterial body is considered. The crack is assumed to be in material 2 and terminating at the interface between the two materials (see Fig. 17) and the body is subjected to a uniform tension p. Appropriate Dirichlet boundary conditions are enforced to arrest any rigid body motion. A structured quadrilateral mesh (50×100) with 5 layers of elements replaced with the scaled boundary finite element method is used for this study. Figure 18 shows the stress in the $y-$direction (σ_{yy} ahead of the crack tip). The results from the present formulation compared favorably with the stresses computed using a very refined finite element model with a conforming mesh.

Next, the case of a crack deflecting into the material is considered. A crack impinging the interface between two dissimilar materials may advance by either propagating along the interface or deflecting into the material. The

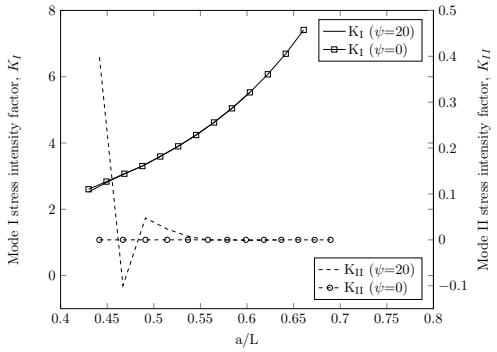

Figure 19: The variation of mode I and mode II stress intensity factor for various crack growth increments. The crack increment is set in advance and the direction of the propagation is based on maximum hoop stress criteria. .

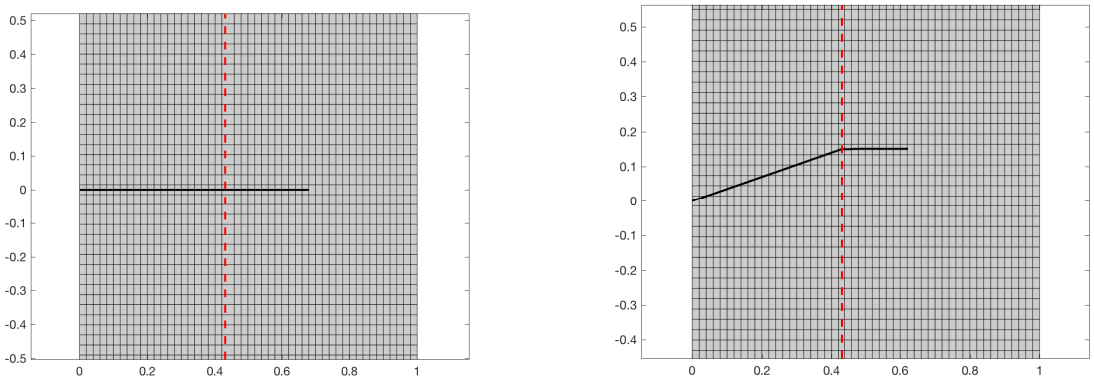

(a) $\psi = 0^\circ$ (b) $\psi = 20^\circ$

Figure 20: Crack trajectory for a crack terminating at the interface and further propagation into material 1 for two different inclination of the crack, $\psi = 0^\circ$ and ψ =20°. The solid black line denotes the crack and dotted line denotes the location of the material interface.

competition between these two scenarios has been thoroughly dealt in the literature [113, 114]. The material properties are assumed to be $E_2 = 100E_1$. The initial crack is assumed to be in material 2 and deflects into the material 1 as it propagates.

Figure 19 shows the variation of the stress intensity factors (mode I and mode II) with crack length a/L. The influence of the initial orientation of the crack is also shown. Since the loading is mode I, the crack propagates in a straight line. For a crack impinging at an angle ψ, initially K_{II} is not zero and hence the crack advances at an angle that is not equal to zero. However, due to the f tensile loading, K_{II} progressively becomes zero as the crack eventually propagates in a straight line. The crack propagation direction is based on the maximum hoop stress criteria. The crack trajectory is shown in Fig. 20 for two different inclination of the crack, $\psi = 0^\circ$ and ψ =20°. In this example, 5 layers of FE mesh is replaced with the scaled boundary domain.

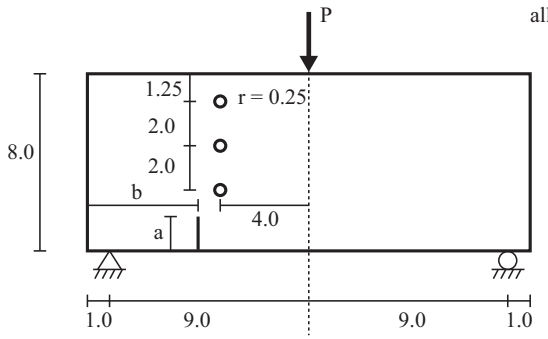

CASE	a	b
I	1.5	5.0
II	1.0	4.0

Figure 21: Cracked beam with three holes.

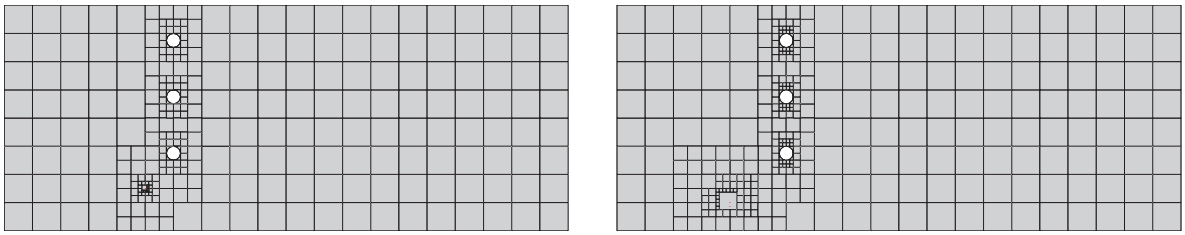

(a) Case I (b) Case II

Figure 22: Initial meshes of the cracked beam with three holes.

6.2. Crack propagation in a beam with three holes

A well-known numerical benchmark for crack propagation problems, the cracked beam with three holes [e.g. 19, 115, 21] under three-point bending condition is considered (Fig. 21). The load is $P = 4.45$N. The dimensions are given in the figure. The beam is made of polymethylcrylate (PMMA). The material properties are: Young's modulus $E = 29 \times 10^6$kPa and Poisson's ratio $\nu = 0.3$. Two cases, I and II, as indicated in Fig 21 are considered. The simulations were carried out under plane stress conditions.

In both cases, the beams are discretised using hybrid polygon-quadtree meshes as shown in Fig. 22a and Fig. 22b. For Case I , the mesh has 438 cells of which 320 are the square cells and 78 are irregular polygons (including the crack cell). In Case II, the mesh has 476 cells of which 354 are square cells and 122 are irregular polygons. A crack incremental length of $\Delta a = 0.5$mm is adopted in the simulations in both cases.

The final meshes for both Case I and Case II are shown in Fig. 23a and Fig. 23b, respectively. It is observed the bulk of the cells in the mesh are still square cells and there is only a minimal increase in the number of arbitrary sided polygons (generally along the crack paths). The initial position of the crack affects the trajectory of the crack propagation. In Case I, the crack initially curved towards the bottom hole. The crack then deviates from its initial path and deflects towards the the middle hole. In Case II, the crack steadily curves towards the middle hole. The simulated crack trajectories in both cases showed good agreement with the experimental results reported by Bittencourt et al. [19] and the finite element simulation of Azocar et al. [21] as shown in Fig. 24.

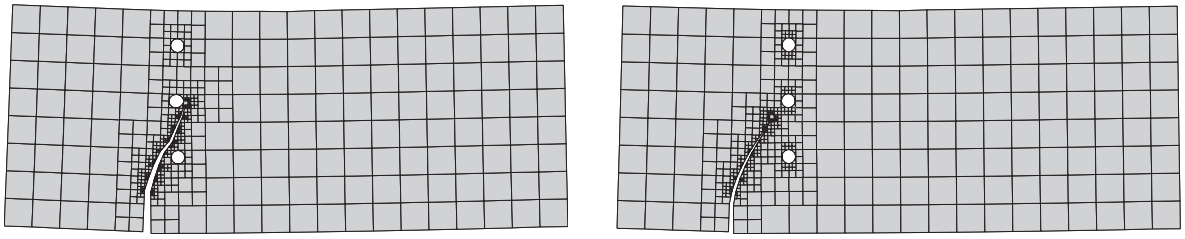

(a) Case I (b) Case II

Figure 23: Final crack paths for cracked beam with three holes.

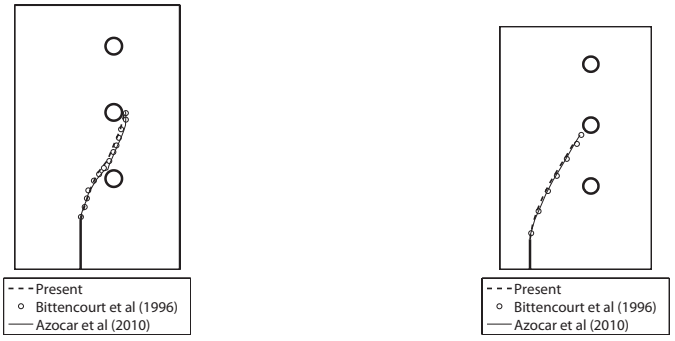

(a) Case I (b) Case II

Figure 24: Comparison of predicted crack paths for the cracked beam with three holes with published results in the literature.

6.3. Impact on a PMMA specimen with a crack emanating from a hole

This example involves the dynamic fracture of a PMMA specimen during a split Hopkinson pressure bar test [116]. For the simulation, the material properties of PMMA reported in [116] are: Young's modulus $E = 3300$MPa, Poisson's ratio $\nu = 0.42$ and density $\rho = 1180\text{kgm}^{-3}$. A dynamic fracture simulation is performed under plane strain conditions. The crack velocity history reported by Fedelinski [117] is specified. The crack is stationary between $0 \leq t \leq 200\mu$s. It then propagates at a velocity $c = 210\text{ms}^{-1}$ between $200\mu\text{s} < t < 270\mu$s and finally stops propagating between $270\mu s \leq t \leq 320\mu$s. Thereafter, the crack propagates again at a velocity of $c = 160\text{ms}^{-1}$ until $t = 500\mu$s. The impact loads, σ_1 and σ_2, at the vertical edges of the plate are applied according to the dynamic input reported in [117].

Figure 26 shows the hybrid quadtree-polygon mesh of the specimen. The hybrid mesh has 472 cells comprising of 1 crack cell, 419 square cells and 52 irregular polygonal cells. The dynamic fracture analysis is carried out using a time step of $\Delta t = 5\mu s$.

Figure 27 shows the stress intensity factor history of the crack. The dynamic stress intensity factors computed by the scaled boundary finite element method were observed to agree reasonably well with those computed with the boundary element method by Fedelinski [117].

The crack propagation path predicted using the scaled boundary finite element method is shown in Fig. 28. The crack initially curves at an angle of approximately 340$^{\text{o}}$ from the horizontal axis. The crack then reorients itself and propagates along the horizontal axis when $t \geq 320\mu s$. When compared with the boundary element simulations of [117],

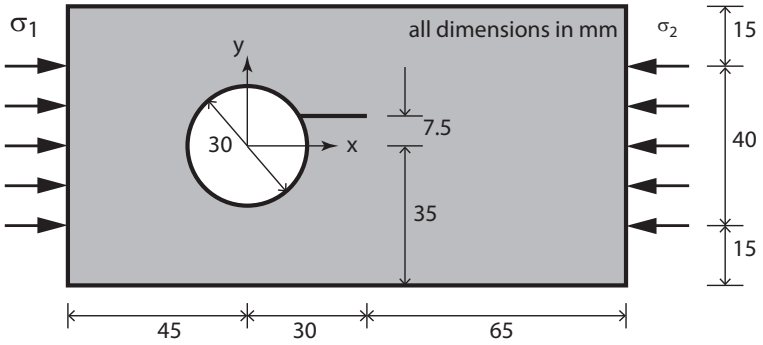

Figure 25: PMMA specimen subjected to impact loads at both ends.

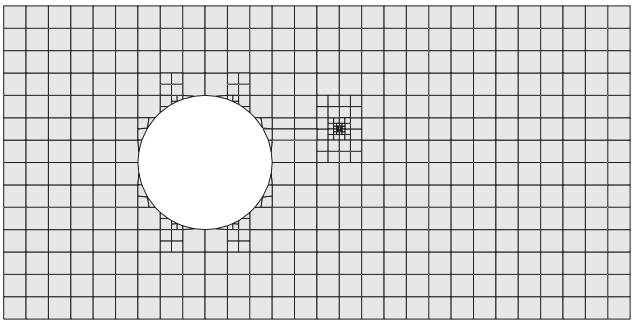

Figure 26: Hybrid mesh of PMMA specimen subjected to impact loads at both ends.

good agreement is observed. The final mesh of the PMMA specimen at the end of the simulation is shown in Fig. 29. The number of cells has increased to 2191. Only 531 of these are irregular polygons. The remaining 1660 cells are square cells.

6.4. Fatigue crack propagation

The fatigue fracture of the Arcan specimen [118] subjected to mixed-mode loading shown in Fig. 30a is considered. The initial crack length at the notch tip a_0 is 2.997 mm and the thickness of the specimen is 1.6 mm. The specimen is made of aluminum (AA2024-T351) with material properties: Young's modulus $E = 73.1$GPa, Poisson's ratio $\nu = 0.33$, Paris exponent $m = 2.9$ and Paris constant $C = 5.3 \times 10^{-11}$. Plane stress conditions are assumed.

An external cyclic loading P with a constant amplitude ratio of $R = \frac{P_{\max}}{P_{\min}} = 0.1$ is applied at a loading angle α measured from the horizontal axis. The magnitude of the external load is first determined by a static analysis so that the initial equivalent stress intensity factor of the crack is $K_{\text{eq}}^{(\text{ini})} = \sqrt{K_{\text{I}}^2 + K_{\text{II}}^2} = 7.59\text{MPa}\sqrt{\text{m}}$ consistent with the experiments performed by Gaylon et al. [118]. Two loading angles $\alpha = 30^\circ$ and $\alpha = 60^\circ$ are considered.

The specimen is discretised with polygon meshes of arbitrary number of sides. Figure 30b shows the polygon mesh. The mesh has 483 polygons and 1043 nodes. The fatigue fracture analysis is carried out using a crack incremental length of $\Delta a = 3$mm.

Figures 31a and b compare the predicted crack paths with the experimental measurements of Gaylon et al. [118]. For the loading case with $\alpha = 30^\circ$, the predicted crack path compares very well with the experimental result. For the

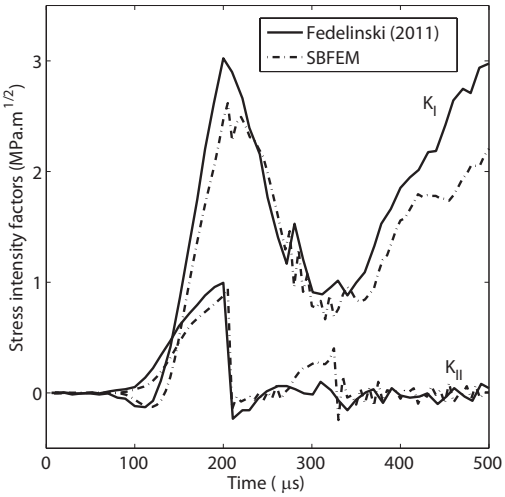

Figure 27: Time history of stress intensity factors for PMMA specimen subjected to impact loads.

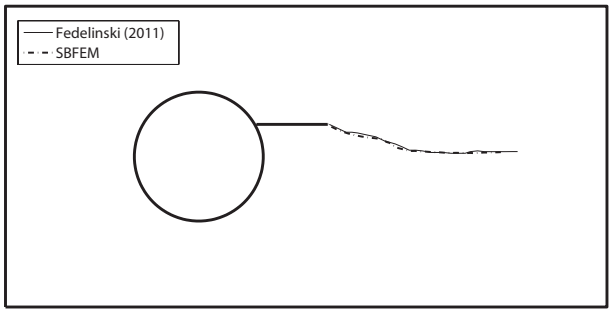

Figure 28: Predicted crack locus of the PMMA specimen subjected to impact loads.

loading case with $\alpha = 60^\circ$, barring the initially vertical crack path observed in the experiments but not captured by the present method, the predicted crack path is almost parallel to the experimental measurements. Figure 32 shows the final polygon meshes for the load cases $\alpha = 30^\circ$ and $\alpha = 60^\circ$.

Figures 33a and b compare the predicted fatigue life of the Arcan specimen with the finite element simulations of [119] for $\alpha = 30^\circ$ and $\alpha = 60^\circ$, respectively. Good agreement is observed. The fatigue life for the load case $\alpha = 30^\circ$ is estimated to be $129,859$ cycles, whereas it was $126,608$ cycles in [119]. For the load case $\alpha = 60^\circ$, the estimated fatigue life is $60,621$ cycles whereas it was $60,855$ cycles in [119].

6.5. Crack propagation in a heterogeneous material

An approach for extending the scaled boundary finite element method to the modelling of heterogeneous materials was conceptualised by Chiong et al. [120] and applied to functionally graded materials. This is achieved by introducing scaled boundary shape functions that are valid for any star convex polygons. The shape functions are continuous, conforming and linearly complete. For a polygon encapsulating a singular point e.g. a crack or a notch, the shape

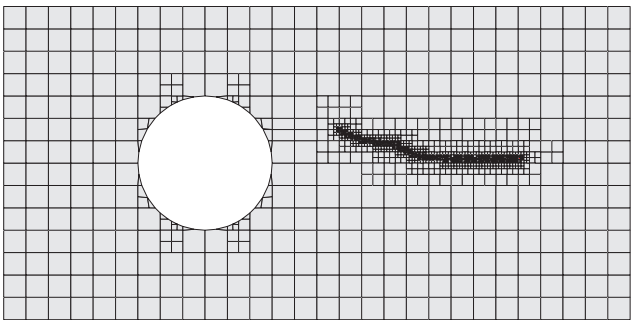

Figure 29: Final mesh of the PMMA specimen subjected to impact loads.

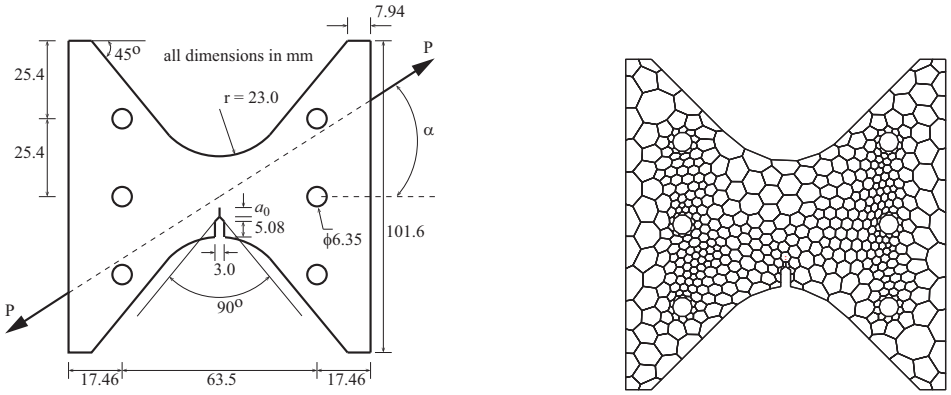

(a) Geometry

(b) Polygon mesh

Figure 30: Arcan specimen.

functions can analytically represent its asymptotic behaviour leading to an accurate procedure to model singularities without the need of local mesh refinement or special techniques.

A functionally graded specimen with two cracks branching from the tip of an existing crack is shown in Fig. 34a. The thickness of the specimen is 6 mm. Crack propagation under a uniform tension is considered. The gradients of the Young's modulus E, Poisson's ratio ν and critical stress intensity factor K_{IC} vary in the $y-$direction and are depicted in Table 4, where $0 \leq \zeta \leq 1$ is the normalised length of the specimen. Plane stress conditions are assumed.

The specimen is discretised using a polygon mesh (Fig. 34b). The mesh has 569 polygons and 1332 nodes. A crack

Table 4: Variation of material properties E, ν and K_{IC} of glass-epoxy functionally graded material.

ζ	0.00	0.17	0.33	0.58	0.83	1.00
E(GPa)	3.0	3.3	5.3	7.3	8.3	8.6
ν	0.35	0.34	0.33	0.31	0.30	0.29
K_{IC}(MPa.m$^{1/2}$)	1.2	2.1	2.7	2.7	2.6	2.6

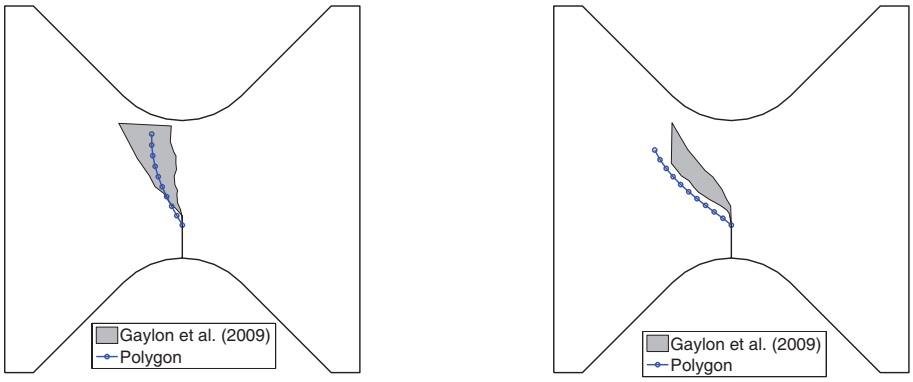

(a) At loading angle $\alpha = 30^\circ$ (b) At loading angle $\alpha = 60^\circ$

Figure 31: Predicted crack paths for Arcan specimen.

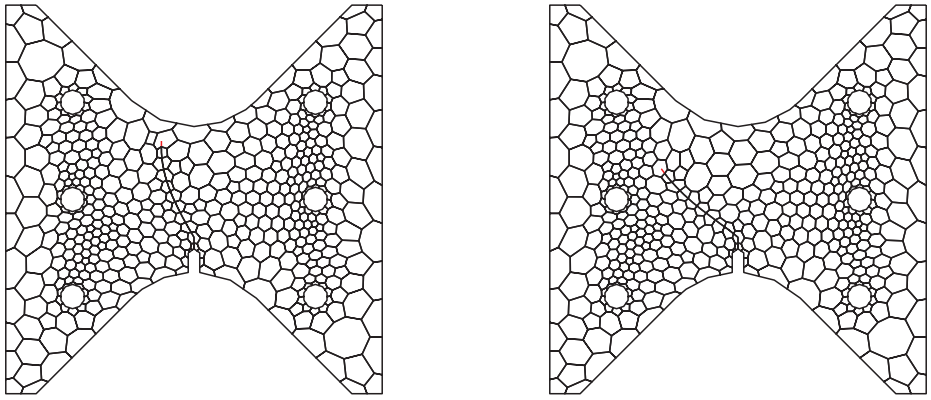

(a) At loading angle $\alpha = 30^\circ$ (b) At loading angle $\alpha = 60^\circ$

Figure 32: Final polygon meshes for Arcan specimen.

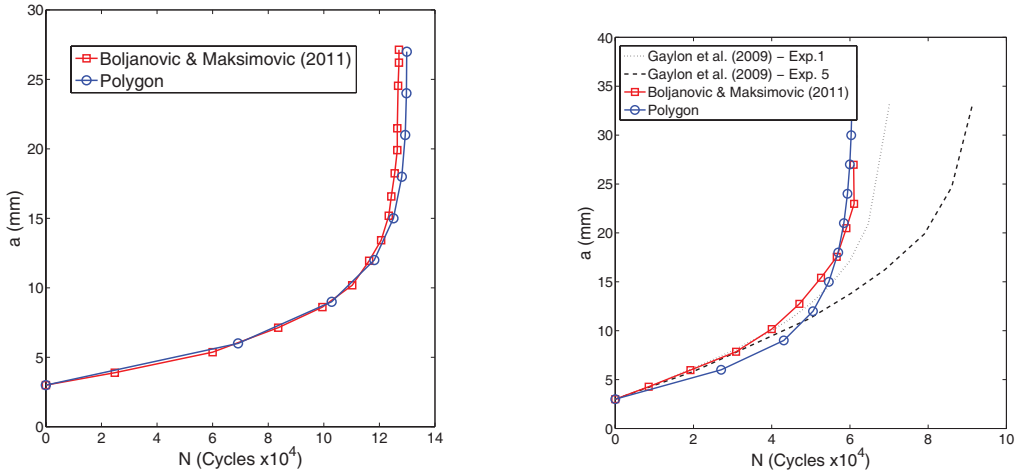

(a) At loading angle $\alpha = 30^\circ$ (b) At loading angle $\alpha = 60^\circ$

Figure 33: Predicted fatigue life for Arcan specimen.

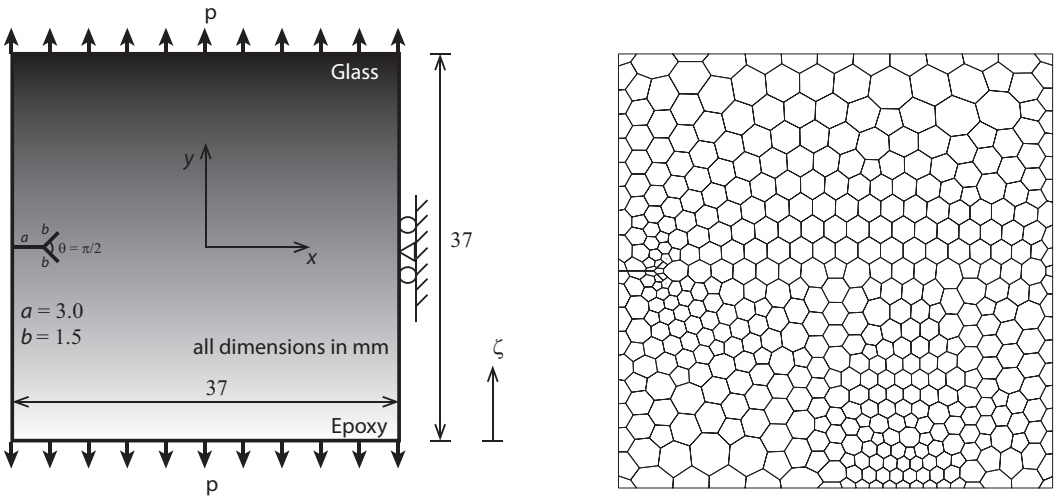

(a) geometry (b) polygon mesh

Figure 34: A functionally graded specimen with branched cracks subjected to uniform tension.

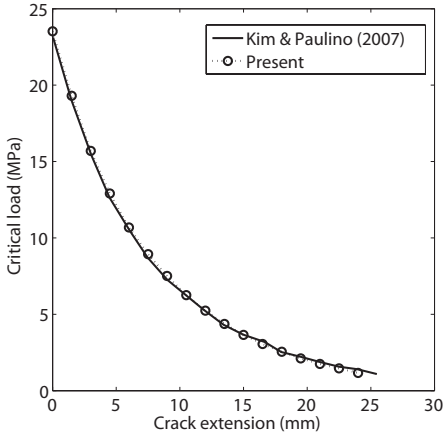

Figure 35: Comparison of predicted critical loads for a functionally graded specimen with branched cracks in Fig. 34.

propagation simulation is carried out using a crack propagation length of $\Delta a = 1.5$mm.

A comparison of the scaled boundary finite element method predicted critical loads in Fig. 35 and the predicted crack paths in Fig. 36a with the FEM simulation reported by Kim and Paulino [31] show very good agreement. Due to the material heterogeneity, the crack propagation between the two crack is unsymmetric when compared with the simulations performed using a homogeneous specimen [31]. The crack tends to be more curved in the region where the magnitude of the Young's modulus is small. Fig. 36b shows the final polygon mesh. The local remeshing algorithm makes only very little change to the overall global mesh structure throughout the entire simulation compared with the FEM results of Kim and Paulino [31].

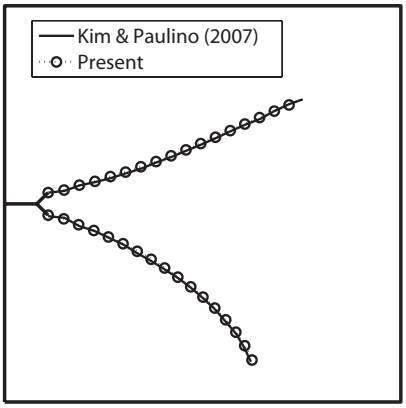

(a) Comparison with the finite element result

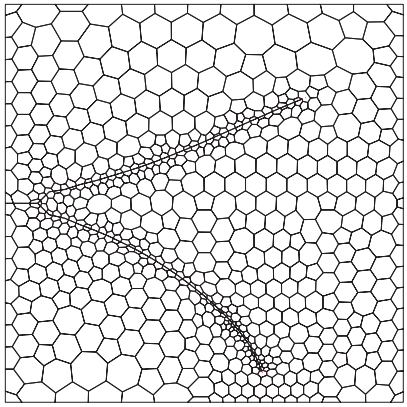

(b) Final polygon mesh

Figure 36: Predicted crack path in functionally graded specimen with branched cracks in Fig. 34.

7. Concluding remarks

The major developments of the scaled boundary finite element method as applied to linear fracture analysis have been reviewed. Applications to the modelling of stress singularities, evaluation of stress intensity factors, $T-$stress, and the simulation of crack propagation are presented. In a single formulation, the scaled boundary finite element method has overcome several key challenges in two-dimensional linear fracture analysis and possesses the following salient features:

1. No analytical asymptotic solutions are required in the definition and in the evaluation of generalised stress intensity factors. It is thus applicable to cracks, V-notches and multi-material corners composed of any number of isotropic and anisotropic materials.
2. The meshing burden is significantly reduced by modelling the region around the singularity point as polygonal subdomain. Only the boundary of the subdomain, excluding the straight crack faces and the material interfaces is discretised. No local mesh refinement around the singularity point is required.
3. All types of stress singularity (real power singularity $r^{-\lambda}$, complex power singularity $r^{-(\lambda_R \pm \mathrm{i}\lambda_I)}$ and power-logarithmic singularity $r^{-\lambda}\ln r$ are modelled analytically in a unified framework.
4. A unified definition of the generalised stress intensity factors for all types of stress singularities is proposed. This definition is consistent with the standard definitions of stress intensity factors for cracks in homogeneous materials and on interfaces of dissimilar isotropic materials.
5. The generalised stress singular intensity factors and the $T-$stress are determined by standard stress recovery techniques as in the finite element method without addressing any singular functions numerically.
6. The use of polygonal subdomain of arbitrary number of edges greatly simplifies the modelling of crack propagation.
7. It can readily be combined with any existing finite element code.

References

[1] M. L. Williams, On the stress distribution at the base of a stationary crack, Journal of Applied Mechanics, ASME 24 (1957) 109–114.

[2] J. R. Rice, A path independent integral and the approximate analysis of strain concentration by notches and cracks, Journal of Applied Mechanics, ASME 35 (1968) 379–386.

[3] J. P. Dempsey, G. B. Sinclair, On the stress singularities in the plane elasticity of the composite wedge, Journal of Elasticity 9 (1979) 373–391.

[4] J. Lindemann, W. Becker, Free-edge stresses around holes in laminates by the boundary finite-element method, Mechanics of Composite Materials 38 (2002) 407–416.

[5] J. R. Rice, A path independent integral and the approximate analysis of strain concentration by notches and cracks, Journal of Applied Mechanics 35 (1968) 379–386.

[6] M. L. Williams, The stress around a fault or crack in dissimilar media, Bulletin of the Seismological Society of America 49 (1959) 199–204.

[7] D. B. Bogy, The plane solution for anisotropic elastic wedges under normal and shear loading, Journal of Applied Mechanics, ASME 39 (1972) 1103–1109.

[8] Z. Suo, Singularities, interfaces and cracks in dissimilar anisotropic media, Proceedings of the Royal Society London Series A-Mathematical, Physical & Engineering Sciences 427 (1990) 331–358.

[9] J. R. Rice, Elastic fracture mechanics concepts for interfacial cracks, Journal of Applied Mechanics, ASME 55 (1988) 98–103.

[10] C. L. Tan, Y. L. Gao, F. F. Afagh, Boundary element analysis of interface cracks between dissimilar anisotropic materials, International Journal of Solids and Structures 29 (1992) 1201–1220.

[11] S. B. Cho, K. R. Lee, Y. S. Choy, R. Yuuki, Determination of stress intensity factors and boundary element analysis for interface cracks in dissimilar anisotropic materials, Engineering Fracture Mechanics 43 (1992) 603–614.

[12] C. Song, Evaluation of power-logarithmic singularities, T-stresses and higher order terms of in-plane singular stress fields at cracks and multi-material corners, Engineering Fracture Mechanics 72 (2005) 1498–1530.

[13] J. P. Dempsey, Power-logarithmic stress singularities at bi-material corners and interface cracks, Journal of Adhesion Science and Technology 9 (1995) 253–265.

[14] C. Hwu, Matrix form near tip solutions of interface corners, International Journal of Fracture 176 (2012) 1–16.

[15] J. Sladek, V. Sladek, Evaluations of the T-stress for interface cracks by the boundary element method, Engineering Fracture Mechanics 56 (1997) 813–825.

[16] R. S. Barsoum, Application of quadratic isoparametric finite elements in linear fracture mechanics, International Journal of Fracture 10 (1974) 603–605.

[17] R. D. Henshell, K. G. Shaw, Crack tip finite elements are unnecessary, International Journal for Numerical Methods in Engineering 9 (1975) 495–507.

[18] P. Bocca, A. Carpinteri, S. Valente, Size effects in the mixed mode crack propagation: Softening and snap-back analysis, Engineering Fracture Mechanics 35 (1990) 159–170.

[19] T. N. Bittencourt, P. A. Wawrzynek, A. R. Ingraffea, Quasi-automatic simulation of crack propagation for 2D LEFM problems, Engineering Fracture Mechanics 55 (1996) 321–334.

[20] P. O. Bouchard, F. Bay, Y. Chastel, Numerical modelling of crack propagation: automatic remeshing and comparison of different criteria, Computer Methods in Applied Mechanics and Engineering 192 (2003) 3887–3908.

[21] D. Azocar, M. Elgueta, M. C. Rivara, Automatic LEFM crack propagation method based on local Lepp-Delaunay mesh refinement, Advances in Engineering Software 41 (2010) 111–119.

[22] S. Courtin, C. Gardin, C. Bézine, H. Hamouda, Advantages of the J-integral approach for calculating stress intensity factors when using the commerical software Abaqus, Engineering Fracture Mechanics 72 (2005) 2174–2185.

[23] J. Kim, G. Paulino, The interaction integral for fracture of orthotropic functionally graded materials: evaluation of stress intensity factors, International Journal of Solids and Structures 40 (2003) 3967–4001.

[24] R. Krueger, Virtual crack closure technique: history, approach and applications, Applied Mechanics Reviews 57 (2004) 109–143.

[25] B. L. Karihaloo, Q. Z. Xiao, Accurate determination of the coefficients of elastic crack tip asymptotic field by a hybrid crack element with p-adaptivity, Engineering Fracture Mechanics 68 (2001) 1609–1630.

[26] B. L. Karihaloo, Q. Z. Xiao, Asymptotic fields at the tip of a cohesive crack, International Journal of Fracture 150 (2008) 55–74.

[27] B. L. Karihaloo, Q. Z. Xiao, Accurate determination of the coefficients of elastic crack tip asymptotic field by a hybrid crack element with p-adaptivity, Engineering Fracture Mechanics 68 (2001) 1609–1630.

[28] Y. Wang, C. Cerigato, H. Waisman, E. Benvenuti, XFEM with high-order material-dependent enrichment functions for stress intensity factors calculation of interface cracks using Irwin's crack closure integral, Engineering Fracture Mechanics 178 (2017) 148–168.

[29] D. Tracey, Finite elements for determination of crack-tip elastic stress intensity factors, Tech. Rep. AD0732837, Army materials and mechanics research center (1971).

[30] S. Atluri, A. Kobayashi, M. Nakagaki, An assumed displacement hybrid finite element model for linear fracture mechanics, International Journal of Fracture (1975) 257–271.

[31] J. H. Kim, G. H. Paulino, On the fracture criteria for mixed-mode crack propagation in functionally graded materials, Mechanics of Advanced Materials and Structures 14 (2007) 227–244.

[32] T. Belytschko, Y. Lu, L. Gu, Element free Galerkin methods, International Journal for Numerical Methods in Engineering 37 (1994) 229–256.

[33] T. Belytschko, Y. Y. Lu, L. Gu, Crack propagation by element-free Galerkin methods, Engineering Fracture Mechanics 51 (1995) 295–315.

[34] T. Belytschko, M. Tabbara, Dynamic fracture using element-free Galerkin methods, International Journal for Numerical Methods in Engineering 39 (1996) 923–938.

[35] M. Flemming, C. Y. A., B. Moran, T. Belytschko, Enriched element-free Galerkin methods for crack tip fields, International Journal for Numerical Methods in Engineering 40 (1997) 1483–1504.

[36] N. Moes, J. Dolbow, T. Belytschko, A finite element method for crack growth without remeshing, International Journal for Numerical Methods in Engineering 46 (1999) 131–150.

[37] M. Stolarska, D. L. Chopp, N. Moes, T. Belytschko, Modelling crack growth by level sets in the extended finite element method, International Journal for Numerical Methods in Engineering 51 (2001) 943–960.

[38] N. Sukumar, J. H. Prevost, Modelling quasi-static crack growth with the extended finite element method. part i: Computer implementation, International Journal of Solids and Structures 40 (2003) 7513–7537.

[39] Q. Z. Xiao, B. L. Karihaloo, X. Y. Liu, Direct determination of SIF and higher order terms of mixed mode cracks by a hybrid crack element, International Journal of Fracture 125 (2004) 207–225.

[40] R. Huang, N. Sukumar, J. H. Prevost, Modeling quasi-static crack growth with the extended finite element method, International Journal of Solids and Structures 40 (2003) 7539–7552.

[41] T. Rabczuk, S. Bordas, G. Zi, A three-dimensional meshfree method for continuous multiple-crack initiation, propagation and junction in statics and dynamics, Computational Mechanics 40 (2007) 473–495.

[42] E. Giner, N. Sukumar, F. D. Denia, F. J. Fuenmayor, Extended finite element method for fretting fatigue crack propagation, International Journal of Solids and Structure 45 (2008) 5675–5687.

[43] X. Zhang, X. Liu, M. W. Lu, Y. Chen, Imposition of essential boundary conditions by displacement constraint equations in meshmesh methods, Communications in Numerical Methods and Engineering 17 (2001) 165–178.

[44] X. Zhuang, C. Augarde, S. Bordas, Accurate fracture modelling using meshless methods, the visibility criterion and level sets: Formulation and 2d modelling, International Journal for Numerical Methods in Engineering 86 (2) (2011) 249–268.

[45] C. L. Richardson, J. Hegemann, E. Sifakis, J. Hellrung, J. M. Teran, An XFEM method for modelling geometrically elaborate crack propagation in brittle materials, International Journal for Numerical Methods in Engineering 88 (2011) 1042–1065.

[46] M. Aliabadi, C. Brebbia, Boundary element formulations in fracture mechanics: a review, Transactions on Engineering Science 13 (1996) 1–17.

[47] T. Panzeca, F. Cucco, S. Terravecchia, Symmetric boundary element method versus finite element method, Computer Methods in Applied Mechanics and Engineering 191 (31) (2002) 3347–3367.

[48] L. Gray, G. Paulino, Symmetric galerkin boundary integral formulation for interface and multi-zone problems, International Journal for Numerical Methods in Engineering 40 (16) (1997) 3085–3101.

[49] C. Song, J. P. Wolf, The scaled boundary finite-element method – alias consistent infinitesimal finite-element cell method – for elastodynamics, Computer Methods in Applied Mechanics and Engineering 147 (1997) 329–355.

[50] C. Song, J. P. Wolf, Semi-analytical representation of stress singularity as occurring in cracks in anisotropic multi-materials with the scaled boundary finite-element method, Computers & Structures 80 (2002) 183–197.

[51] C. Song, F. Tin-Loi, W. Gao, A definition and evaluation procedure of generalized stress intensity factors at cracks and multi-material wedges, Engineering Fracture Mechanics 77 (12) (2010) 2316–2336.

[52] C. Li, C. Song, H. Man, E. Ooi, W. Gao, 2D dynamic analysis of cracks and interface cracks in piezoelectric composites using the SBFEM, International Journal of Solids and Structures 51 (11-12) (2014) 2096–2108.

[53] C. Li, E. Ooi, C. Song, S. Natarajan, Sbfem for fracture analysis of piezoelectric composites under thermal load, International Journal of Solids and Structures 52 (2015) 114–129.

[54] J. Sladek, V. Sladek, S. Krahulec, C. Song, Crack analyses in porous piezoelectric brittle materials by the sbfem, Engineering Fracture Mechanics 160 (2016) 78–94.

[55] Z. Sun, E. Ooi, C. Song, Finite fracture mechanics analysis using the scaled boundary finite element method, Engineering Fracture Mechanics 134 (2015) 330–353.

[56] A. W. Egger, E. N. Chatzi, S. P. Triantafyllou, An enhanced scaled boundary finite element method for linear elastic fracture, Archive of Applied Mechanics (2017) 1–40.

[57] S. R. Chidgzey, A. J. Deeks, Determination of coefficients of crack tip asymptotic fields using the scaled boundary finite element method, Engineering Fracture Mechanics 72 (2005) 2019–2036.

[58] C. Song, A super-element for crack analysis in the time domain, International Journal for Numerical Methods in Engineering 61 (2004) 1332–1357.

[59] A. Müller, J. Wenck, S. Goswami, J. Lindemann, J. Hohe, W.Becker, The boundary finite element method for predicting directions of cracks emerging from notches at bimaterial junctions, Engineering Fracture Mechanics 72 (2005) 373–386.

[60] S. Goswami, W. Becker, Computation of 3-D stress singularities for multiple cracks and crack intersections by the scaled boundary finite element method, International Journal of Fracture 175 (2012) 13–25.

[61] A. A. Saputra, C. Birk, C. Song, Computation of three-dimensional fracture parameters at interface cracks and notches by the scaled boundary finite element method, Engineering Fracture Mechanics 148 (2015) 213–242.

[62] S. Hell, W. Becker, Energy release rates at two perpendicularly meeting cracks by use of the Scaled Boundary Finite Element Method, Procedia Structural Integrity 2 (2016) 2471–2478.

[63] C. Mittelstedt, W. Becker, Efficient computation of order and mode of three-dimensional stress singularities in linear elaelastic by the boundary finite element method, International Journal of Solids and Structures 43 (2006) 2868–2903.

[64] C. Mittelstedt, W. Becker, Semi-analytical computation of 3D stress singularities in linear elasticity, Communications in Numerical Methods in Engineering 21 (2005) 247–257.

[65] S. Hell, W. Becker, Hypersingularities in three-dimensional crack configurations in composite laminates, Proceedings in Applied Mathematics and Mechanics PAMM 14 (2014) 157–158.

[66] W. Mayland, W. Becker, Scaled boundary finite element analysis of stress singularities in piezoelectric multimaterial systems, Proceedings of Applied Mathematics and Mechanics 9 (2009) 9–102.

[67] Z. J. Yang, Fully automatic modelling of mixed-mode crack propagation using scaled boundary finite element method, Engineering Fracture Mechanics 73 (12) (2006) 1711–1731.

[68] Z. J. Yang, A. J. Deeks, Fully automatic modelling of cohesive crack growth using a finite element-saled boundary finite element coupled method, Engineering Fracture Mechanics 74 (16) (2007) 2547–2573.

[69] Z. J. Yang, A. J. Deeks, Modelling cohesive crack growth using a two-step finite element-scaled boundary finite element coupled method, International Journal of Fracture 143 (4) (2007) 333–354.

[70] E. T. Ooi, Z. J. Yang, Modelling multiple cohesive crack propagation using a finite element-scaled boundary finite element coupled method, Engineering Analysis with Boundary Elements 33 (7) (2009) 925–929.

[71] E. T. Ooi, Z. J. Yang, Efficient prediction of size effects using the scaled boundary finite element method, Engineering Fracture Mechanics 77 (6) (2010) 985–1000.

[72] C. Zhu, G. Lin, J. Li, Modelling cohesive crack growth in concrete beams using scaled boundary finite element method based on super-element remeshing technique, Computers and Structures 121 (2013) 76–86.

[73] E. T. Ooi, Z. J. Yang, Modelling dynamic crack propagation using the scaled boundary finite element method, International Journal for Numerical Methods in Engineering 88 (4) (2011) 329–349.

[74] E. T. Ooi, Z. J. Yang, Z. Y. Guo, Dynamic cohesive crack propagation modelling using the scaled boundary finite element method, Fatigue and Fracture of Engineering Materials and Structures 35 (8) (2012) 786–800.

[75] A. J. Deeks, C. E. Augarde, A hybrid meshless local petrov–galerkin method for unbounded domains, Computer Methods in Applied Mechanics and Engineering 196 (2007) 843 – 852.

[76] Y. Q. He, H. T. Yang, A. J. Deeks, Determination of coefficients of crack tip asymptotic fields by an element-free galerkin scaled boundary method, Fatigue and Fracture of Engineering Materials and Structures 35 (2012) 767–785.

[77] S. R. Chidgzey, J. Trevelyan, A. J. Deeks, Coupling of the boundary element method and the scaled boundary finite element method for computation in fracture mechanics, Computers and Structures 86 (2008) 1198–1203.

[78] G. Bird, J. Trevelyan, C. Augarde, A coupled BEM/scaled boundary FEM formulation for accurate computations in linear elastic fracture mechanics, Engineering Analysis with Boundary Elements 34 (6) (2010) 599–610.

[79] E. T. Ooi, Z. J. Yang, A hybrid finite element-scaled boundary finite element method for crack propagation modelling, Computer Methods in Applied Mechanics and Engineering 199 (17-20) (2010) 1178–1187.

[80] E. T. Ooi, Z. J. Yang, Modelling crack propagation in reinforced concrete using a hybrid finite element - scaled boundary finite element method, Engineering Fracture Mechanics 78 (2) (2011) 252–273.

[81] Z. J. Yang, X. F. Wang, D. S. Yin, C. Zhang, A non-matching finite element-scaled boundary finite element coupled method for linear elastic crack propagation modelling, Computers and Structures 153 (2015) 126–136.

[82] S. Natarajan, C. Song, Representation of singular fields without asymptotic enrichment in the extended finite element method, International Journal for Numerical Methods in Engineering 96 (2013) 813–841.

[83] J. B. Li, X. A. Fu, B. B. Chen, C. Wu, G. Lin, Modelling crack propagation with the extended scaled boundary finite element method based on the level set method, Computers and Structures 167 (2016) 50–68.

[84] E. T. Ooi, C. Song, F. Tin-Loi, Z. J. Yang, Automatic modelling of cohesive crack propagation in concrete using polygon scaled boundary finite elements, Engineering Fracture Mechanics 93 (2012) 13–33.

[85] E. T. Ooi, H. Man, S. Natarajan, C. Song, Adaptation of quadtree meshes in the scaled boundary finite element method for crack propagation modelling, Engineering Fracture Mechanics 144 (2015) 101–117.

[86] J. P. Wolf, C. Song, The scaled boundary finite-element method – a primer: derivations, Computers & Structures 78 (2000) 191–210.

[87] A. J. Deeks, J. P. Wolf, A virtual work derivation of the scaled boundary finite-element method for elastostatics, Computation Mechanics 28 (2002) 489–504.

[88] C. Song, A matrix function solution for the scaled boundary finite-element equation in statics, Computer Methods in Applied Mechanics and Engineering 193 (2004) 2325–2356.

[89] A. Tabarraei, N. Sukumar, Extended finite element method on polygon and quadtree meshes, Computer Methods in Applied Mechanics and Engineering 197 (2008) 45–438.

[90] T. Fries, A. Byfut, A. Alizada, K. W. Cheng, A. Schroder, Hanging nodes and XFEM, International Journal for Numerical Methods in Engineering 86 (2011) 404–430.

[91] S. Natarajan, C. Song, Representation of singular fields without asymptotic enrichment in the extended finite element method, International Journal for Numerical Methods in Engineering (2013) 813–841.

[92] S. R. Chidgzey, A. J. Deeks, Determination of coefficients of crack tip asymptotic fields using the scaled boundary finite element method, Engineering Fracture Mechanics 72 (2005) 2019–2036.

[93] S. Chen, Q. Li, Y. Liu, Z. Xue, Mode III 2-D fracture analysis by the scaled boundary finite element method, Acta Mechanica Solida Sinica 26 (2013) 619–628.

[94] J. Y. Liu, F. L. Xu, B. K. Ning, H. Fan, Evaluation of the T-stress and the higher order terms of the elastic crack based on the SBFEM, Advanced Materials Research 838-841 (2014) 2275–2278.

[95] F. L. Xu, J. Y. Liu, B. K. Ning, F. He, Evaluation of the higher order terms of the wedge splitting specimen based on the SBFEM, Applied Mechanics and Materials 477-478 (2014) 25–29.

[96] R. Dieringer, W. Becker, A new scaled boundary finite element formulation for the computation of singularity orders at cracks and notches in arbitrarily laminated composites, Composite Structures 123 (2015) 263–270.

[97] C. Li, H. Man, C. Song, W. Gao, Fracture analysis of piezoelectric materials using the scaled boundary finite element method, Engineering Fracture Mechanics 97 (2013) 52–71.

[98] C. Li, L. Tong, 2D fracture analysis of magnetoelectroelastic composites by the SBFEM, Composite Structures 132 (2015) 984–994.

[99] R. Behnke, M. Mundil, C. Birk, M. Kaliske, A physically and geometrically nonlinear scaled-boundary-based finite elemen formulation for fracture in elastomers, International Journal for Numerical Methods in Engineering 99 (2014) 966–999.

[100] S. Hell, W. Becker, The scaled boundary finite element method for the analysis of 3D crack interaction, Journal of Computational Science 9 (2015) 76–81.

[101] M. Chowdhury, C. Song, W. Gao, Highly accurate solutions and Padé approximants of the stress intensity factors and T-stress for standard specimens, Engineering Fracture Mechanics 144 (2015) 46–67.

[102] C. Song, F. Tin-Loi, W. Gao, Transient dynamic analysis of interface cracks in anisotropic bimaterials by the scaled boundary finite-element method, International Journal of Solids and Structures 47 (2010) 978–989.

[103] T. Matsumto, M. Tanaka, R. Obara, Computation of stress intensify factors of interface cracks based on interaction energy release rates and BEM sensitivity analysis, Engineering Fracture Mechanics (2000) 683–702.

[104] E. T. Ooi, C. Song, F. Tin-Loi, Z. J. Yang, Polygon scaled boundary finite elements for crack propagation modelling, International Journal for Numerical Methods in Engineering 91 (3) (2012) 319–342.

[105] C. Talischi, G. H. Paulino, A. Pereira, I. F. M. Menezes, Polymesher: a general-purpose mesh generator for popolygon elements written in matlab, Structural and Multidisciplinary Optimization 45 (3) (2012) 309–328.

[106] S. Dai, C. Augarde, C. Du, D. Chen, A fully automatic polygon scaled boundary finite element method for modelling crack propagation, Engineering Fracture Mechanics 133 (2015) 163–178.

[107] M. Shi, H. Zhong, E. T. Ooi, C. Zhang, C. S, Modelling of crack propagation of gravity dams by scaled boundary polygons and cohesive crack model, International Journal of Fracture 183 (1) (2013) 29–48.

[108] E. T. Ooi, M. Shi, C. Song, F. Tin-Loi, Z. J. Yang, Dynamic crack propagation simulation with scaled boundary polygon eelement and automatic remeshing technique, Engineering Fracture Mechanics 103 (2013) 1–21.

[109] E. T. Ooi, S. Natarajan, C. Song, F. Tin-Loi, Crack propagation modelling in functionally graded materials using scaled boundary polygons, International Journal of Fracture 192 (1) (2015) 87–105.

[110] P. Reddy, H. J. Montas, H. Samet, A. Shirmohammadi, A quadtree-based triangular mesh generation for finite element analysis of heterogeneous spatial data, ASAE Annual International Meeting 300 ((01-3072)) (2001) 1–25.

[111] E. T. Ooi, S. Natarajan, C. Song, E. H. Ooi, Crack propagation modelling in concrete using the scaled boundary finite element method with hybrid polygon-quadtree meshes, International Journal of Fracture 203 (1-2) (2017) 135–157.

[112] E. T. Ooi, S. Natarajan, C. Song, E. H. Ooi, Dynamic fracture simulations using the scaled boundary finite element method on hybrid polygon-quadtree meshes, International Journal of Impact Engineering 90 (2016) 154–164.

[113] M.-Y. He, J. Hutchinson, Crack deflection at an interface between dissimilar elastic materials, International Journal of Solids and Structures (1989) 1053–1067.

[114] M.-Y. He, J. Hutchinson, Kinking of a crack out of an interface, Journal of Applied Mechanics (1988) 270–278.

[115] S. Phongthanapanich, P. Dechaumphai, Adaptive Delaunay triangulation with object-oriented programming for crack propagation analysis, Finite Elements in Analysis and Design 40 (2004) 1753–1771.

[116] D. Gregoire, H. Maigre, J. Rethore, A. Combescure, Dynamic crack propagation under mixed-mode loading - comparison between experiments and x-fem simulations, International Journal of Solids and Structures 44 (2007) 6517–6534.

[117] P. Fedelinski, Computer modelling of dynamic fracture experiments, Key Engineering Materials 454 (2011) 113–125.

[118] S. E. Gaylon, S. R. Arunachalam, J. Greer, M. Hammond, S. A. Fawaz, Three dimensional crack growth prediction, in: M. J. Bos (Ed.), Proceedings of the 25th Symposium of the International Committee on Aeronautical Fatigue (ICAF 2009), Bridging the Gap Between Theory and Operational Practice, Rotterdam, the Netherlands, 2009, pp. 1035–1068.

[119] S. Boljanovic, S. Maksimovic, Analysis of crack growth propagation under mixed-mode loading, Engineering Fracture Mechanics 78 (2011) 1565–1576.

[120] I. Chiong, E. T. Ooi, C. Song, F. Tin-Loi, Scaled boundary polygons with application to fracture analysis of functionally graded materials, International Journal for Numerical Methods in Engineering 98 (2014) 562–589.